

1 **Effects of pH and Ca exchange on the structure and redox state of synthetic Na-birnessite**

2 Chiara Elmi^{1,2,*}, Jeffrey E. Post¹, Peter J. Heaney³, Eugene S. Ilton⁴

3 ¹*Department of Mineral Sciences, National Museum of Natural History, Smithsonian Institution,*

4 *Washington, DC, 20013-7012, USA; ²Current address: Department of Geology and*

5 *Environmental Sciences, James Madison University, Harrisonburg, VA 22807, USA;*

6 ³*Department of Geosciences, Penn State University, 540 Deike Building, University Park, PA*

7 *16802, USA; ⁴Pacific Northwest National Laboratory, 902 Battelle Blvd., Richland, WA 99352,*

8 *USA*

9

10 *Corresponding author: Chiara Elmi, elmicx@jmu.edu

11

12 **Abstract.** Birnessite-like minerals are among the most common Mn oxides in surficial soils and
13 sediments, and they mediate important environmental processes (*e.g.*, biogeochemical cycles,
14 heavy metal confinement) and novel technological applications (*e.g.*, water oxidation catalysis).
15 Ca is the dominant interlayer cation in both biotic and abiotic birnessites, especially when they
16 form in association with carbonates. The current study investigated the structures of a series of
17 synthetic Ca-birnessite analogs prepared by cation-exchange with synthetic Na-birnessite at pH
18 concentrations from 2 to 7.5. The resulting Ca-exchanged birnessite phases were characterized
19 using powder X-ray diffraction and Rietveld refinement, Fourier transform infrared
20 spectroscopy, Raman spectroscopy, X-ray photoelectron spectroscopy, and scanning and
21 transmission electron microscopy. All samples synthesized at pH values greater than 3 exhibited
22 a similar triclinic structure with nearly identical unit-cell parameters. The samples exchanged at
23 pH 2 and 3 yielded hexagonal structures, or mixtures of hexagonal and triclinic phases. Rietveld

24 structure refinement and X-ray photoelectron spectroscopy showed that exchange of Na by Ca
25 triggered reduction of some Mn^{3+} , generating interlayer Mn^{2+} and vacancies in the octahedral
26 layers. The triclinic and hexagonal Ca-birnessite structures described in this study were distinct
27 from Na- and H-birnessite, respectively. Therefore, modeling X-ray absorption spectra of natural
28 Ca-rich birnessites through a mixing of Na- and H-birnessite endmembers will not yield an
29 accurate representation of the true structure.

30

31 INTRODUCTION

32 Phylломanganates are highly reactive layer-structure Mn oxide minerals found in a wide
33 variety of geological settings and are important constituents in soils and sediments. In particular,
34 phylломanganates having a birnessite-like structure readily participate in redox and cation-
35 exchange reactions and exhibit high adsorption capacities for a variety of organic pollutants and
36 toxic metallic ions (Le Goff et al. 1996; Manning et al. 2002; Feng et al. 2007; Lopano et al.
37 2007; Fleeger et al. 2013; Kwon et al. 2013; Shumlas et al. 2016). Layer Mn oxides have low
38 point-of-zero charges (PZC) and therefore possess a relatively high negative charge at near-
39 neutral pH values (Tan et al. 2008; Wang et al. 2010). Because of this high reactivity,
40 phylломanganates play an important role in controlling the concentration of trace metal ions in
41 soils, sediments, and natural water systems (Post 1999; Tan et al. 2008). They also have been
42 identified as promising heterogeneous compounds for water-oxidation catalysis (Sauer and
43 Yachandra 2002; Feng et al. 2007; Jiao and Frei 2010; Wiechen et al. 2012; Frey et al. 2014).

44 Birnessite was first described by Jones and Milne (1956) as a natural phase discovered in
45 Aberdeenshire, Scotland with a chemical formula of $\text{Na}_{0.7}\text{Ca}_{0.3}\text{Mn}_7\text{O}_{14} \cdot 2.8\text{H}_2\text{O}$. Subsequently,
46 numerous natural phases with “birnessite-like” structures have been described, including

47 ranciéite (Post et al. 2008), takanelite (McKenzie 1971; Golden 1986), and lagalyite (Witzke et
48 al. 2017). They commonly occur as fine-grained, poorly crystalline aggregates and coatings,
49 making the studies of their structures and behaviors challenging. Additionally, various synthetic
50 birnessite-like structures containing almost every alkali and alkaline earth element, as well as
51 many of the transition metals, have been synthesized (*e.g.*, McKenzie 1971; Golden 1986) in
52 attempts to elucidate the structural and chemical features of birnessite-like phyllomanganates
53 (*e.g.*, Post and Veblen 1990; Kuma et al. 1994; Drits et al. 1997; Lanson et al. 2000; Post et al.
54 2003; Feng et al. 2004; Händel et al. 2013) and their reactivities (*e.g.*, Lanson et al. 2000;
55 Manceau et al. 2002; Feng et al. 2007; Lopano et al. 2007, 2011; Wang et al. 2010, 2012;
56 Landrot et al. 2012; Kwon et al. 2013; Lefkowitz et al. 2013, 2013; Yin et al. 2013; Fischel et al.
57 2015; Hinkle et al. 2016; Zhao et al. 2016; Fischer et al. 2018). Laboratory studies have also
58 demonstrated that formation of birnessite-like phases can be initiated, or enhanced, by certain
59 microbes and fungi (Tebo et al. 2004; Webb et al. 2005; Grangeon et al. 2010; Santelli et al.
60 2011), and it is therefore likely that biologically mediated phyllomanganates are important in
61 natural systems.

62 The birnessite structure is constructed of stacked layers of nominally $\text{Mn}^{4+}\text{-O}_6$ octahedra;
63 substitution of Mn^{3+} or other lower valence cations and/or vacancies for Mn result in a net
64 negative charge on the octahedral sheets (Fig. 1). The charge is offset by addition of large uni- or
65 divalent cations (*e.g.* Na^+ , Ba^{2+} , K^+ , Ca^{2+}) into the interlayer region, along with water molecules.
66 Birnessite-like phases with predominantly Mn^{4+} exhibit overall hexagonal (trigonal) or near-
67 hexagonal symmetry. As the proportion of Mn^{3+} increases, the associated Jahn-Teller distortions
68 lower the symmetry to triclinic (Silvester et al. 1997; Ling et al. 2018). Birnessite-like structures
69 exhibit a characteristic $\sim 7 \text{ \AA}$ repeat in the layer stacking direction. In buserite phases, a double

70 layer of water molecules expands the layer spacing to ~ 10 Å. Recent studies of naturally
71 occurring birnessite/buserite-like phases from fresh-water environments revealed Ca to be the
72 predominant interlayer cation, sometimes associated with Mg, Ba, and/or K (Bargar et al. 2005;
73 Tan et al. 2010).

74 It is generally assumed that naturally occurring Ca-rich phylломanganates form by a
75 biologically mediated, or enhanced, process (Bargar et al. 2005). Interestingly, the water-
76 oxidation reaction that is a critical step in photosynthesis is catalyzed within the enzyme
77 photosystem II (PSII) by a μ -oxido bridged CaMn_4 cluster known as the oxygen-evolving-
78 complex (OEC) (Umena et al. 2011; Zhang et al. 2015; Yamaguchi et al. 2017). Inspired by the
79 composition of the OEC, scientists have explored the water-oxidation capacity of ranciéite, the
80 Ca-rich member of the birnessite group (Sauer and Yachandra 2002; Andreiadis et al. 2011; Hou
81 2011; Wiechen et al. 2012; Frey et al. 2014; Zaharieva et al. 2016). Some of these water-
82 oxidation experiments demonstrated that birnessite-like minerals require the presence of calcium
83 in their structures to reach maximum catalytic activity (Wiechen et al. 2012).

84 Because of the widespread association of Ca with natural phylломanganates and the
85 critical role of birnessite-like clusters in water-oxidation catalysis, we undertook an investigation
86 of interactions of aqueous Ca with synthetic birnessite-like phases. A primary goal of the study
87 was to explore the chemical and structural modifications occurring in synthetic Na-birnessite
88 when transformed by cation exchange into Ca-birnessite in aqueous solutions over a range of pH
89 and Ca concentrations that are similar to those found in many natural systems. In particular, this
90 paper aims to determine whether the Ca-birnessite structure is distinct from other varieties of
91 birnessite, and to gain insights into the mechanism(s) by which cation-exchange transforms

92 birnessite-like structures. Additionally, the synthesized Ca-birnessites are compared with natural
93 Ca-rich birnessite-like phases, including ranciéite.

94

95 **MATERIALS AND METHODS**

96 *Synthesis of Na-birnessite and hexagonal birnessite*

97 Triclinic birnessite was prepared following the synthesis for Na-birnessite outlined in
98 Lopano et al. (2007), based on the synthesis procedures described by Golden (1986). In the
99 present synthesis, 250 ml of 5.5 M NaOH solution and 200 ml of 0.5 M MnCl₂·4H₂O solution
100 were chilled overnight at 4 °C. The Na-birnessite precipitate was formed by stirring the NaOH
101 and MnCl₂·4H₂O solutions at room temperature and then bubbling oxygen into the mixture with
102 a Pyrex™ coarse porosity fritted cylinder (pore size = 40-60 μm) for five hours. Analytical grade
103 chemicals and deionized water were used for the synthesis. The precipitate was centrifuged in
104 conical polypropylene centrifuge tubes (capacity = 50 ml) and rinsed five times with 40 ml of
105 deionized water. The sample was then left to air-dry on a watch glass at room temperature
106 overnight. After 24 hours, the sample was dried at 30 °C for 5 minutes to effect a complete
107 transformation from Na-buserite to Na-birnessite.

108 Hexagonal birnessite was synthesized by reacting ~100 mg of dried triclinic Na-
109 birnessite in 250 ml of 0.001 M HCl for 24 hours. The sample was then centrifuged 5 times with
110 deionized water, and left to air-dry overnight. Previous studies have shown, and our EDS
111 analyses confirmed, that the hexagonal birnessite had no Na, or metal cations other than Mn, in
112 the structure.

113

114 *Ca- exchange experiments*

115 100 mg samples of triclinic Na-birnessite were placed in 600 ml glass beakers with 200
116 ml of 1 M, 0.1 M, and 0.01 M CaCl₂ · 2H₂O solutions initially at pH 6.5 and pH 7.5 for ~24 h.
117 Analytical grade chemicals and deionized water were used for the Ca exchange experiments. The
118 beakers were covered with Parafilm® for the duration of the experiments. After 24 hours, each
119 Ca-exchanged sample was centrifuged in conical polypropylene centrifuge tubes (capacity = 50
120 ml) and rinsed five times with 40 ml of deionized water. The samples were then air-dried on a
121 watch glass at room temperature overnight, and then dried at 30 °C for 5 minutes to effect a
122 complete transformation from Ca-buserite to Ca-birnessite. In order to monitor the rate of the
123 cation exchange, sample aliquots were removed from the reaction vessel at 5 min intervals for
124 the first hour and then every hour until the end of the run for the experiment at pH 6.5 using 1 M
125 Ca²⁺.

126 The exchange experiments were repeated following the same procedure above at pH 5.5,
127 pH 4, pH 3 and pH 2. In these experiments, the initial pH of Ca solutions was adjusted with 0.1
128 M HCl; the pH of the reaction solution was also measured at the end of each exchange
129 experiment. For all exchange reactions other than at pH 3, the final pH increased by less than 0.5
130 units; the final values for the exchanges at pH 3 ranged between 4.9 and 5.6.

131

132 *Scanning electron microscopy*

133 Uncoated Ca-birnessite samples were mounted on carbon tape adhered to an aluminum
134 stub and analyzed with scanning electron microscopy (SEM) using a field emission source (FEI
135 Apreo) equipped with an EDAX Octane Silicon Drift energy-dispersive X-ray spectroscopy
136 (EDS) detector (Scanning Electron Microscopy Laboratory, National Museum of Natural
137 History, Smithsonian Institution). Backscattered electron (BSE) images were collected, and

138 energy dispersive X-ray spectroscopy (EDS) was used to determine the chemical composition
139 and homogeneity of the Ca-birnessite samples (with beam current of 1.6 nA). The images were
140 collected and analyses performed in low vacuum (0.31 torr) at an accelerating voltage of 15 kV.
141 The data were processed using the Noran System Six 3 (NSS 3) software.

142

143 *X-ray diffraction (XRD)*

144 All prepared samples were characterized by powder X-ray diffraction using a Rigaku II
145 D/MAX-RAPID microdiffractometer (Smithsonian Institution, Department of Mineral Sciences)
146 equipped with a graphite monochromator and a curved image plate area detector. A Mo tube (50
147 kV, 40 mA) was used as the X-ray source with a 0.3 mm collimator. Small (~1 mm) balls of
148 sample were mounted with water-based glue on tips of glass fibers, and during exposure to the
149 X-ray beam, the sample was oscillated between -30° to +30° phi to minimize the effects of
150 sample heterogeneity and preferred orientation. The full set of Debye-Scherrer diffraction rings
151 from the imaging plate data were integrated using Rigaku-provided software, and interpretation
152 of XRD patterns was performed using the JADE 9 software package. Additionally, synchrotron
153 XRD data sets for selected samples (pH: 7.5, 6.5, 3, and 2) were collected at the Advanced
154 Photon Source (Beam Line 13-BM-C) for samples mounted in 1 mm (ID) polyimide capillaries
155 using 30 s exposures with a MAR CCD 165 area detector and $\lambda = 0.828438 \text{ \AA}$. The synchrotron
156 image data were processed to 2D intensity-versus-2Theta patterns using Dioptas (Prescher and
157 Prakapenka 2015).

158 Rietveld refinements (Rietveld, 1969) were performed for selected samples using the
159 General Structure Analysis System-II (GSAS-II) software (Toby and Von Dreele 2013).
160 Diffraction data generated by a LaB₆ standard (NIST SRM 660a) were used to calibrate peak

161 profile parameters that described instrumental broadening for the Rigaku and synchrotron
162 experiments. For all samples, diffraction peak profiles were fit with a pseudo-Voigt function as
163 parameterized by Thompson, et al. (1987), with asymmetry correction by Finger et al. (1994),
164 and microstrain anisotropic broadening terms by Stephens (1999).

165 The structure refinements were initiated using the triclinic Na- birnessite structure of
166 Lopano et al. (2007), and the starting atom positions for the H-birnessite refinement were derived
167 from Ling et al. (2015). The (001) peak was omitted due to its high relative intensity and
168 problems with integrating the diffraction images near the direct beam. The background
169 parameters, scale factor, unit-cell parameters, peak profile coefficients, and appropriate atom
170 parameters were allowed to vary. The background intensities were fitted with a Chebyshev
171 function using 5-7 terms.

172

173 *Transmission electron microscopy (TEM)*

174 Samples of Ca-birnessite formed from exchange of triclinic Na-birnessite with solutions
175 containing 1.0 and 0.1 M Ca²⁺ at pH 2 and 0.1 M Ca²⁺ at pH 7.5 were prepared for TEM analysis
176 by lightly grinding powders in ethanol in an agate mortar to disaggregate the particles. The
177 ethanol-birnessite suspension then was ultrasonicated for 60 s, followed by immersion of a holey
178 carbon TEM grid into the suspension. The grain mounts were analyzed using a ThermoFisher
179 Scientific Talos F200X TEM with a field-emission gun (FEG) source operating at 200 kV in the
180 Materials Characterization Laboratory at Penn State University.

181

182 *FT-IR spectroscopy*

183 Transmission spectra of the Na-, H-, and Ca-birnessite samples were obtained at room
184 temperature over the range 350–6000 cm^{-1} using a Thermo Scientific Nicolet 6700 Fourier-
185 Transform infra-red spectrometer (Smithsonian Institution, Department of Mineral Sciences).
186 KBr pellets were prepared from mixtures of approximately 1 mg of Mn oxide and 250 mg of
187 KBr that were ground in a mill for at least 1 min, and pressed for 2 min. The resolution was set at
188 3.86 cm^{-1} , and 120 scans were co-added for each spectrum. During data collection, the sample
189 chamber was purged with air scrubbed for water and CO_2 . Background spectra for samples did
190 not show significant shifts over time. The Omnic 8 software (Nicolet) was used for data
191 collection.

192

193 *Raman spectroscopy*

194 Raman spectra for the Na-, H-, and Ca-birnessite samples were collected using a
195 HORIBA LabRam HR Evolution equipped with deep-depleted thermoelectrically cooled CCD
196 (charge coupled device) array detector and an optical microscope (Smithsonian Institution,
197 Department of Mineral Sciences). All measurements were made at 25 °C. All powders were
198 pressed onto glass discs to obtain an approximately flat surface for Raman analysis. Sample
199 areas were analyzed using an Olympus 50× objective, an integration time of 30 s, and at a
200 spectral resolution of 2 cm^{-1} using a 784 nm solid state laser. Four acquisitions per spot were set
201 to improve the signal-to-noise ratio. Low laser power was used to minimize sample alteration by
202 heating. The spectrometer was fitted with a holographic notch filter and grating (600 g/mm), and
203 was controlled using the Horiba LaBSPEC6 software.

204

205 **X-ray photoelectron spectroscopy (XPS)**

Revision 4

206 XPS analyses were performed to determine concentrations of Mn^{4+} , Mn^{3+} , and Mn^{2+} for Ca-
207 birnessite samples exchanged using 0.01 M Ca^{2+} at pH 7.5, 3, and 2. Because of limited
208 instrument availability, samples were selected that represented the range of pH conditions and
209 different structure symmetries. Data collection and fitting procedures were followed as reported
210 by Ilton et al. (2016). Powder samples were covered with a strip of conductive copper tape and
211 pressed with clean borosilicate glass blocks onto copper stubs. XPS measurements were
212 performed with a Physical Electronics Quantera Scanning X-ray Microprobe. This system uses a
213 focused monochromatic Al $K\alpha$ X-ray (1486.7 eV) source for excitation and a spherical section
214 analyzer. The instrument has a 32 element multichannel detection system. The X-ray beam is
215 incident normal to the sample and the photoelectron detector is at 45° off-normal. High energy
216 resolution spectra were collected using a pass-energy of 69.0 eV with a step size of 0.125 eV.
217 For the Ag $3d_{5/2}$ line, these conditions produced a FWHM of $0.92 \text{ eV} \pm 0.05 \text{ eV}$. The binding
218 energy (BE) scale is calibrated using the Cu $2p_{3/2}$ feature at $932.62 \pm 0.05 \text{ eV}$ and Au $4f_{7/2}$ at
219 $83.96 \pm 0.05 \text{ eV}$. The sample experienced variable degrees of charging. Low energy electrons at
220 $\sim 1 \text{ eV}$, $20\mu\text{A}$ and low energy Ar^+ ions were used to minimize this charging. Measurements of the
221 $\text{Mn}2p$, $\text{Mn}3s$, $\text{Mn}3p$, $O1s$, $Cl1s$, and various alkali and alkaline Earth lines were conducted with a
222 step size of 0.1 eV, an analysis area of $300 \times 700 \mu\text{m}$, and pass energies (PE) of 20 or 40 eV.
223 The low sensitivity of the $\text{Mn}3s$ line resulted in measurements only with PE = 40 eV. Survey
224 scans were conducted at PE = 160 eV and step size = 0.5 eV. XPS spectra were fit by non-linear
225 least squares after Shirley background subtractions with the CasaXPS curve resolution software
226 package. Gaussian/Lorentzian contributions to line shapes were numerically convoluted with a
227 Voigt function.

228

229 RESULTS

230 *SEM and EDS Analyses*

231 SEM images (Fig. 2) show that all of the Na-birnessite and Ca-exchanged birnessite
232 samples exhibited the same flake-like morphology. Morphology and crystal size (~2 μm in
233 diameter) did not change significantly from the starting Na-birnessite following exchange at
234 different Ca concentrations and pH conditions.

235 The EDS analyses confirmed that the exchange of Ca for Na was complete for all
236 samples within detection limits for Na (nominally 0.05 wt.%). The degree of Ca uptake as a
237 function of pH and Ca^{2+} concentration is displayed in Figure 3. For experiments at pH 4 and
238 above, the number of Ca cations exchanged per Mn atom was approximately half that of Na in
239 the starting Na-birnessite (from ~0.30 Na/Mn to ~0.16 Ca/Mn), as expected for a charge-neutral
240 exchange, *i.e.* one Ca^{2+} for every 2 Na^+ . Moreover, the exchange of Ca for Na was rapid. EDS
241 analyses revealed that full exchange had occurred within 5 min after Na-birnessite powders were
242 added to a 1 M Ca^{2+} solution at pH 6.5. In contrast, birnessite samples exchanged at pH 2 and 3
243 exhibited lower levels of exchange (except at pH 3 when the Ca^{2+}_{aq} concentration was ≥ 1 M). In
244 solutions at pH 3 and with 0.1 M and 0.01 M Ca^{2+} – and for all concentrations of Ca^{2+}_{aq} prepared
245 at pH 2 – the number of Ca cations per Mn atom was approximately 1/3 of that for the samples
246 exchanged at higher pH (~0.05 Ca/Mn rather than ~0.16 Ca/Mn) (Fig. 3).

247

248 *XRD and Rietveld Refinements*

249 The powder XRD patterns for products from 1 M Ca-exchange experiments at various
250 pH values are plotted in Figure 4, and they indicate similar triclinic structures for all pH values
251 greater than 2. Rietveld refinements for our synthetic Na- and H-birnessite endmembers yielded

252 structures and unit-cell parameters consistent with those previously reported (Post et al. 2002;
253 Ling et al. 2015). On the other hand, when Ca^{2+} exchanged in a 1:2 ratio with Na^+ at pH 3 to 7.5,
254 the X-ray diffraction patterns for the resulting Ca-birnessite differed sufficiently from those of
255 Na-birnessite that a new unit cell was required for Rietveld analysis. Viable unit-cell parameters
256 for these Ca-birnessite samples were ascertained using the computer program Crystal Cracker
257 (Leinenweber, 2019), and confirmed by performing a successful LeBail fit using GSASII. For
258 the initial stages of refinement for these Ca-birnessite samples, only the octahedral Mn and O
259 atoms were included in the structure model. Difference Fourier maps were calculated for the
260 interlayer region to locate electron density corresponding to $\text{H}_2\text{O}/\text{Ca}$ molecules.

261 For all structures that experienced a 1:2 $\text{Ca}^{2+}:\text{Na}^+$ exchange, the difference maps revealed
262 significant electron density within the interlayer near $z = 0.6$ (and by symmetry, $z = 0.4$). The
263 location and the diffuse nature of the electron density suggested that it corresponded to a
264 disordered $\text{Ca}/\text{H}_2\text{O}$ position. There was a lesser area of electron density centered at
265 approximately $(0, 0, 0.66)$ that might arise from Ca coordinated to the octahedral sheets (*i.e.*,
266 above and below possible Mn vacancies), as occurs in natural ranciéite (Post et al. 2008). The
267 observed $\text{H}_2\text{O}/\text{Ca}$ site was added to the structure model (as O), and its position and occupancy
268 factor were allowed to vary during subsequent refinement cycles. A Ca site was added that
269 corresponded to the electron density peak on the difference map at $(0, 0, 0.66)$; attempts to refine
270 an occupancy factor did not yield consistent results, most likely because of the low occupancy
271 (~ 0.07 , assuming 7% Mn vacancies and consistent with the measured XPS Mn^{2+} composition)
272 and strong correlations in the refinement between the occupancy factor and background
273 coefficients. Consequently, the Ca site occupancy factor was fixed to a value of 0.07. The refined
274 unit-cell parameters for Ca-birnessite samples synthesized under a range of pH and Ca^{2+}

275 concentration conditions are listed in Table 1. A structure drawing for synthesized Na- and Ca-
276 birnessite is shown in Figure 1.

277 Rietveld refinements for all structures that experienced a 1:2 $\text{Ca}^{2+}:\text{Na}^+$ exchange yielded
278 triclinic unit cells that are significantly different from that of Na-birnessite, but nearly identical
279 to each other. On the other hand, samples exchanged at pH 3 using 0.1 M and 0.01 M Ca^{2+} were
280 mixtures of a predominantly hexagonal phase and a minor triclinic phase (Table 1). The structure
281 for samples exchanged with 0.01 M Ca^{2+} at pH 2 was refined using a hexagonal unit cell in space
282 group *P*-3 (Fig. 1), closely similar to that of hexagonal H-birnessite Ling et al. (2015). At pH 2
283 and higher concentrations of dissolved Ca^{2+} (1.0 and 0.1 M Ca^{2+}), however, refinements required
284 a triclinic cell, but one in which the *a* and *b* unit-cell parameters matched those of hexagonal H-
285 birnessite, but the values for the α and β unit-cell angles did not. The final Rietveld refinement
286 difference plot reveals an additional peak at $d \sim 1.86 \text{ \AA}$. It is weaker or absent in other
287 preparations at similar pH conditions. The peak could be an impurity not related to the Ca-
288 birnessite structure. Final observed and calculated diffraction patterns for representative Rietveld
289 refinements for triclinic and hexagonal structures are shown in Figure 5.

290

291 *FTIR and Raman spectra*

292 Ling et al. (2017) demonstrate that FTIR spectroscopy can successfully differentiate
293 triclinic from hexagonal birnessites. FTIR spectra of triclinic Na-birnessite show three distinct
294 peaks in the Mn-O vibrational mode region, but only two modes are obvious for the higher
295 symmetry hexagonal, or near-hexagonal, structures. Likewise, Raman spectra for triclinic and
296 hexagonal birnessites show differences in the number and positions of peaks (Julien 2003; Hsu et
297 al. 2011; Yang et al. 2015; Boumaiza et al. 2019). FTIR (Fig. 6) and Raman (Fig. 7) spectra for

298 several of the Ca-birnessite samples prepared in this study show clear trends as a function of
299 solution pH. The FTIR and Raman spectra for Ca-birnessite samples that underwent a 1:2
300 $\text{Ca}^{2+}:\text{Na}^{+}$ exchange at higher pH were similar to that of Na-birnessite, whereas those prepared at
301 lower Ca^{2+} concentrations at pH 3 and all samples at pH 2 were analogs to that of H-birnessite.
302 Consequently, the FTIR and Raman results reinforce our conclusions based on X-ray diffraction
303 – that fully exchanged Ca-birnessites at higher pH are triclinic, whereas Ca-birnessites
304 exchanged at low pH are hexagonal, or nearly so.

305

306 *HRTEM and SAED*

307 High-resolution TEM and selected-area electron diffraction also supported the conclusion
308 that Ca-birnessite crystals synthesized at higher pH and Ca concentrations were structurally
309 distinct from those produced at pH 2. Ca-birnessite samples generated from the reaction of
310 triclinic Na-birnessite with solutions at pH 2 and either 0.1 or 1 M CaCl_2 exhibited SAED
311 patterns with hexagonal symmetry (Z.A. [001]) that typically were free of streaks or
312 superstructures (Fig. 8A,B). High-resolution TEM images of these crystals (Fig. 8) generally
313 exhibited little in the way of microstructural defects, although faint superstructure reflections
314 halfway along the $[100]^*$ and $[010]^*$ directions were apparent, suggesting a doubled
315 superperiodicity involving the 100 and 001 planes in local areas (Fig. 8C). Rarely, crystals with
316 heavy structural disorder were observed, as evidenced by streaking in SAED patterns and
317 irregular modulations among the (100) and (010) planes in HRTEM images.

318 In contrast, TEM analysis of Ca-birnessite crystals exchanged from Na-birnessite at pH
319 7.5 revealed a structural character that was more closely analogous to that of triclinic birnessite.
320 The angle between $[100]^*$ and $[010]^*$ deviated sufficiently from hexagonality that

321 superimposition of the same SAED pattern on itself with a 60° rotation yielded a clear doubling
322 of diffraction spots. Consequently, these diffraction patterns were best indexed to the $C\bar{1}$ cell
323 (Fig. 9A,B). Additionally, these crystals commonly revealed superstructure reflections at $1/3$
324 $[200]^*$, as was also observed in SAED patterns of the starting triclinic Na-birnessite but never in
325 our hexagonal birnessite. HRTEM images and fast-Fourier transforms of these triclinic crystals
326 likewise displayed stronger superperiodicities and streaking than were observed in the hexagonal
327 birnessites prepared at pH 2 (Fig. 9C).

328

329 *XPS*

330 Following Ilton et al. (2016), the $3p$ XPS spectra were fitted to determine the Mn
331 oxidation state concentrations for Ca-birnessite samples exchanged using 0.01 M Ca^{2+} at pH 7.5,
332 3, and 2. Ilton et al. (2016) conclude that the $3p$ data are most representative of the bulk sample
333 and yield results that best match those for Mn oxide standards. The Mn oxidation states
334 determined for the samples measured in this study are given in Table 2. Interestingly, the average
335 oxidation states for the phases in Table 2 are not significantly different, despite major changes in
336 the relative abundances of the different Mn oxidation states. The relatively large estimated errors
337 for the pH 3 values can be attributed to the observation that this sample was a mixture of triclinic
338 and hexagonal phases, as discussed below. Relationships between $\text{Mn}^{2+,3+}$ content and structural
339 symmetry are plotted in Figure 10.

340

341 **DISCUSSION**

342 *Effects of Ca substitution on the triclinic birnessite structure*

343 **Variations among triclinic unit cells of birnessite.** The crystal structures for Ca-
344 birnessite samples exchanged above pH 3 for all Ca²⁺ concentrations are triclinic, and they are
345 similar to each other but different from that of Na-triclinic birnessite, as is the Ca-birnessite
346 produced at pH 3 and 1 M Ca²⁺. The unit-cell parameters determined by the Rietveld refinements
347 for these triclinic Ca-birnessite phases were identical within experimental error. Similarly, the
348 analyzed Ca concentrations for these Ca-birnessite samples were essentially the same, with
349 Ca/Mn = 0.16 (Fig. 3), indicating a 1:2 charge-balanced exchange of Ca²⁺ for Na⁺. Moreover,
350 when Na-birnessite samples were immersed in pH 6.5 solutions at 1 M Ca²⁺ and analyzed by
351 XRD at 5-min intervals during the exchange reaction for 1 hr, the unit-cell parameters exhibited
352 no measurable changes with time. These observations strongly support the existence of a triclinic
353 Ca-birnessite structure that is distinct from other triclinic varieties of birnessite. Specifically, the
354 unit-cell lengths and angles refined here reveal a markedly smaller deviation from hexagonal
355 symmetry than is the case with Na-, K-, or Ba-birnessite (Table 1), consistent with the inferences
356 of Ling et al. (2018). We hypothesize that this structure may closely correspond to natural
357 triclinic Ca-birnessites that form at circumneutral pH and a range of Ca concentrations.

358 Previous studies have shown that cation exchange of K, Mg, Ba, Cs, and Li for Na in
359 triclinic birnessite produce distinctly different triclinic unit cells (Chukhrov et al. 1979; Golden
360 1986; Lopano et al. 2007; Fleeger et al. 2013). The refined crystal structures reported for these
361 birnessites exhibit similar *a* and *b* unit-cell parameters, suggesting that the Mn-O octahedral
362 sheets are relatively undistorted by the interlayer cations when they reside in the middle of the
363 interlayer (*z* ~ 0.5). Rather, hydrated cations of different sizes, charges, and occupancies are
364 accommodated primarily through minor translations of neighboring octahedral sheets, as is
365 reflected in differences in unit-cell angles and layer spacings (the *c*-axis length) (Table 1).

366 **Mn reduction induced by Ca exchange.** Although our refinement of triclinic Na-
367 birnessite revealed full occupancy for octahedral Mn (as is consistent with previous reports), all
368 of the triclinic Ca-birnessite analyses in the present study yielded octahedral vacancies ranging
369 from 3 to 10%, with an average of 7%. The variations exhibited for the Mn occupancy factor did
370 not correlate with differences in experimental conditions, but likely represent uncertainties in the
371 Rietveld results because of correlations among the Mn occupancy factor, background
372 coefficients, and thermal parameters. These non-unitary occupancies suggest that concomitant
373 with the exchange of Ca for Na is a loss of some Mn from the octahedral sheets, most likely by
374 reduction of some Mn³⁺ to Mn²⁺, which goes into solution. This scenario is in agreement with
375 Kong (2017), who showed the release of Mn into solution following exchange of 1.0 M Ca²⁺
376 with Na-birnessite at near neutral pH. Additionally XPS analyses of the Ca-birnessite sample
377 exchanged from Na-birnessite at pH 7.5 using 0.1 M Ca²⁺ showed a decrease in the Mn³⁺/Mn⁴⁺
378 value, relative to that of Na-birnessite, from 0.61 (Ilton et al. 2016) to 0.45. The XPS data also
379 indicate that ~7% of the total Mn is Mn²⁺, which might be absorbed onto the surface, and/or in
380 the interlayer with the Ca.

381 The FTIR and Raman spectra (Figs. 6 and 7) provide additional support for the
382 interpretation that Mn³⁺ and/or Mn⁴⁺ are reduced during Ca exchange with Na-birnessite. The
383 Raman and FTIR spectra for samples exchanged at pH values greater than 3.0 are consistent with
384 those for triclinic birnessite phases (Ling et al. 2017). One notable difference, however, is a ~12
385 nm shift of the Mn-O stretch Raman line at ~650 nm to higher wavenumbers following exchange
386 of Ca with Na-birnessite. Our observations comparing Raman spectra for several well-
387 characterized phyllosomanganate phases suggest that the ~650 nm Raman line shifts to lower
388 wavenumbers with increasing values of Mn³⁺/Mn⁴⁺, presumably as a consequence of the longer

389 average Mn^{3+} -O bonds relative to those with Mn^{4+} . The Raman spectra shown here, therefore,
390 are consistent with a decrease in $\text{Mn}^{3+}/\text{Mn}^{4+}$ as Ca exchanged for Na, and the magnitude of the
391 shift is essentially the same for all of the triclinic Ca-birnessite samples.

392 **Maintaining charge balance.** How is charge balance achieved in the birnessites that
393 experienced a 1:2 $\text{Ca}^{2+}:\text{Na}^+$ exchange? If we adopt an average occupancy of 0.93 for octahedral
394 Mn, as was typical of our refinements, then 7% of the octahedral sites are vacant ($\square_{\text{occ}} = 0.07$). If
395 we further accept the XPS-derived $\text{Mn}^{3+}/\text{Mn}^{4+}$ value of 0.45 ($\text{Mn}^{3+} = 29\%$, $\text{Mn}^{4+} = 64\%$, and Mn^{2+}
396 $= 7\%$), then $\text{Mn}^{3+}_{\text{occ}} = 0.29$ and $\text{Mn}^{4+}_{\text{occ}} = 0.64$. Since the multiplicity of Mn in S.G. C-1 is 2, that
397 leads to 0.14 vacancies per unit cell and 0.58 Mn^{3+} cations per unit cell. Pauling's second rule
398 shows that an octahedral sheet fully occupied by Mn^{4+} is charge balanced [$3 \times 4/6 = 2$].
399 Therefore, the charge deficit caused by substitutions of either vacancies or Mn^{3+} cations for Mn^{4+}
400 yields a net negative charge per unit cell. Since triclinic birnessite has one octahedral sheet per
401 unit cell, summing the charge deficits in Ca-birnessite [$(-4) \times 0.14$ for \square plus $(-1) \times 0.58$ for
402 $\text{Mn}_{\text{oct}}^{3+}$] yields a negative charge of -1.22 for each octahedral sheet. This calculation assumes
403 that Mn^{2+} cations are too large to occupy the octahedral sites (Post 1999), and it does not
404 consider that some of the Mn^{3+} might be in interlayer sites.

405 Do the measured concentrations of interlayer cation content accommodate the negative
406 sheet charge? EDS analyses for the birnessites exchanged at higher pH yielded 0.15 Ca/Mn (Fig.
407 3) for a contribution of +0.60 per unit cell, and XPS analyses indicated $\sim 0.14 \text{Mn}^{2+}$ for a
408 contribution of +0.28 per unit cell for a total charge of $\sim +0.88$ per unit cell. The charge
409 discrepancy between sheet and interlayer might suggest that interlayer Mn^{3+} or H_3O^+ occupies
410 interlayer sites and/or that OH^- replaces some of the O atoms in the octahedral sheets. If we
411 assume that no Mn^{2+} was lost to solution, that no Mn^{3+} resides in the interlayer, and that H^+ in

Revision 4

412 some fashion balances the octahedral charge deficit, then the resulting formula for this Ca-
413 exchanged birnessite at pH 7.5 is $(\text{Ca}^{2+}_{0.15}, \text{Mn}^{2+}_{0.07}, \text{H}^{+}_{0.13}) (\text{Mn}^{3+}_{0.29}, \text{Mn}^{4+}_{0.64}, \square_{0.07}) \text{O}_2 \cdot x\text{H}_2\text{O}$.
414 In comparison, the formula for the starting Na-birnessite before exchange was approximately
415 $(\text{Na}^{+}_{0.29}, \text{Mn}^{2+}_{0.02}, \text{H}^{+}_{0.06}) (\text{Mn}^{3+}_{0.39}, \text{Mn}^{4+}_{0.61}) \text{O}_2 \cdot 0.75\text{H}_2\text{O}$.

416 These calculations suggest that some of the divalent cations occupy positions near the
417 center of the interlayer. The negative charge induced by 0.14 vacancies per octahedral sheet in
418 Ca-birnessite would be balanced by 0.28 ($\text{Ca}^{2+} + \text{Mn}^{2+}$), which is a little more than half that
419 determined by EDS and XPS analyses, which yielded $\sim 0.30 \text{Ca}^{2+}$ and 0.14Mn^{2+} , respectively,
420 per unit cell. Alternatively, some of the vacancies might be compensated by Mn^{3+} .

421 The fact that the average 0.14 vacant octahedral sites per unit cell determined by our
422 refinements is equal to the 0.14Mn^{2+} per unit cell measured by XPS suggests the possibility that
423 all of the Mn that moved into the interlayer as Mn^{2+} are located above and below the resulting
424 vacancies. Any remaining interlayer cations likely occupy positions closer to the middle of the
425 interlayer region where they are coordinated to water molecules and octahedral O atoms.
426 Because of the positional disorder and diffuse electron density, it is not clear how meaningful is
427 the occupancy factor refined for the interlayer Ca/H₂O site, but the value is sufficiently large to
428 more than account for what would be predicted if it is fully occupied by H₂O molecules and all
429 of the Ca^{2+} cations. The precise positions of these Ca^{2+} , and possibly some Mn^{2+} , or Mn^{3+} ,
430 cations near $z = 0.5-0.6$ in the interlayer might correlate to the local arrangement of Mn^{3+} and
431 vacancies in the adjacent octahedral sheets. Our refinements offered no indications for long-
432 range order of either the octahedral vacancies or Mn^{3+} cations, and the diffuse electron densities
433 revealed in difference Fourier maps suggest positional disorder among the interlayer cations and
434 water molecules.

435

436 *Effects of Ca substitution on the hexagonal birnessite structure*

437 **Increasing hexagonality with increasing H⁺:Ca²⁺ ratios.** The final products of the
438 exchange reactions at pH 2 and 3 depended upon the pH and the Ca²⁺ concentration. For the
439 exchanges with 0.1 M Ca²⁺ at pH 3, the XRD and Raman data revealed a mixture with
440 approximately 1/3 triclinic and 2/3 hexagonal birnessite structures, based on Rietveld refinement.
441 The unit-cell parameters for the two phases are listed in Table 1. The Ca-birnessite formed using
442 0.01 M Ca at pH 3 was similarly mixed, but with only ~25% triclinic Ca-birnessite. However, all
443 of the Ca-birnessites produced at pH 2 exhibited hexagonal, or near hexagonal, symmetries,
444 according to our XRD, FTIR, Raman, and TEM analyses. Interestingly, the Rietveld refinement
445 for the sample exchanged using 0.1 M Ca²⁺ yielded an excellent fit for a structure with *a*, *b*, and *c*
446 unit-cell parameters similar to those for hexagonal H-birnessite, but the α angle in particular
447 (94.25°) differed from the expected value of 90° (Table 1). Apparently, the Mn-O octahedral
448 sheets in this Ca-birnessite structure have near-hexagonal symmetry, consistent with the
449 observed *a*, *b*, and γ values, but the stacking of the sheets gives rise to triclinic symmetry. The
450 hexagonal symmetry indicated by the Raman spectrum for this sample (Fig. 5) is consistent with
451 that of the average local environment around Mn in the octahedral sheet.

452 The chemical analyses also indicate that the Ca-birnessite phases produced at lower pH
453 values are distinct from those generated by a 1 Ca²⁺ for 2 Na⁺ exchange at higher pH. For Ca-
454 birnessites formed at pH 3 using 0.1 and 0.01 M Ca²⁺, the measured Ca/Mn ratios were only
455 ~0.07 rather than ~0.16, and the Ca/Mn values for all of the samples exchanged at pH 2 ranged
456 between 0.03 and 0.06. The smaller number for interlayer Ca²⁺ is consistent with a hexagonal

457 birnessite structure in which the negative charge on the octahedral sheet is balanced by higher
458 concentrations of interlayer Mn^{2+} .

459 Indeed, our Rietveld refinement for the sample exchanged with 0.01 M Ca^{2+} at pH 2
460 yielded a nominally triclinic unit-cell that was very close to that expected for a hexagonal
461 structure; the value for α was 91.8° , instead of the expected 90° . When the refinement was
462 performed using space group $P-3$, the goodness-of-fit values did not differ significantly from
463 those using the $C-1$ triclinic cell. The atomic parameters determined with S.G. $P-3$ were nearly
464 identical to those of hexagonal H-birnessite, including the refined Mn occupancy of ~ 0.90 . This
465 occupancy is significantly lower than those refined for the triclinic Ca-birnessite structures at
466 higher pH ($\text{Mn}_{\text{occ}} \sim 0.94$). For the exchanges at pH 2, the XPS results (Table 2) indicate the
467 reduction of Mn^{3+} to Mn^{2+} , resulting in octahedral vacancies as Mn^{2+} migrated into the interlayer
468 (Lanson et al. 2000). Difference Fourier maps of these Ca-birnessites exchanged at very low pH
469 revealed electron densities above and below the octahedral sites, consistent with interlayer Mn^{2+}
470 (and possibly some Ca^{2+} and Mn^{3+}) in tridentate coordination with vacant octahedral sites. The
471 loss of the larger Mn^{3+} , relative to Mn^{4+} , from the octahedral sheets also is consistent with the
472 change in the average Mn-O distances determined from the Rietveld refinements, which are
473 ~ 1.95 Å for the triclinic Ca-birnessite structures, but only ~ 1.92 Å for the hexagonal Ca-
474 birnessite.

475 **Mechanism of Ca-induced reduction of Mn^{3+} .** Although it is well-established that
476 dissolved transition metals will reduce $\text{Mn}^{3+/4+}$ in birnessite to Mn^{2+} through direct electron
477 transfer from the transition metal (Feng et al. 2004, 2007; Fischer 2010; Fischel et al. 2015), the
478 mechanism by which the exchange of Na^+ by Ca^{2+} causes reduction of Mn^{3+} cannot involve the
479 oxidation of Ca^{2+} . The Ca-O interaction would further lengthen and destabilize the Mn^{3+} -O bond,

480 favoring a disproportionation reaction as described by Silvester et al. (1997): $2\text{Mn}^{3+} \rightarrow \text{Mn}^{2+} +$
481 Mn^{4+} . The Mn^{2+} cation is sterically too large for the octahedral sheet and relocates either to a
482 tridentate position above the resulting octahedral vacancy, inducing at least some of the Ca to
483 relocate to the $z \sim 0.5$ plane, or else the Mn^{2+} is lost to solution. As a result of the decrease in
484 octahedral strain, the triclinic distortion in Ca-birnessite is markedly lower than is observed in
485 Na-, K-, Ba-, or Cs-birnessites (Lopano et al. 2007, 2009).

486 When pH is very low, the Ca^{2+} cations must compete with H^+ cations for those Jahn-
487 Teller distorted O anions. Thus, in our experiments, the transition from triclinic to hexagonal
488 structures occurred for all exchanges at pH 2 (H^+ concentration = 0.01 M), and for sufficiently
489 low concentrations of Ca^{2+} (0.1 and 0.01 M Ca^{2+}) at pH 3 (H^+ concentration = 0.001 M).
490 Tellingly, when the Ca^{2+} concentration was 1.0 M at pH 3, the full 1:2 Ca-for-Na exchange
491 occurred, and the final structure was triclinic. Thus, at certain H/Ca values the smaller and more
492 mobile H^+ cations gain a competitive advantage, and a tipping point occurs when Ca
493 concentrations fall between 0.1 and 1.0 M Ca^{2+} at pH 3.

494

495 *Superstructures*

496 SAED patterns of the Ca-birnessites exchanged at pH 7.5 typically showed faint
497 superstructure reflections at $1/3 [200]^*$ (Fig. 9B). Drits et al. (1998) also report superstructure
498 reflections in SAED patterns for their synthetic Ca-birnessite, but different from those we
499 observed. In one variant, $a_{\text{super}} = 3a$, $b_{\text{super}} = 3b$, and $c_{\text{super}} = 4c$. Another variant represents an
500 interstratification of two cells with $a_{\text{super}} = 3/2 (a - b)$, $b_{\text{super}} = 4b$, and $c = 4c$ alternating with
501 $a_{\text{super}} = 3/2(a + b)$, $b_{\text{super}} = -4b$, and $c_{\text{super}} = 4c$. The disparity in superperiodicities that we
502 observed relative to the complex superstructures reported by Drits et al. (1998) may be explained

503 by differences in the preparation of the Ca-birnessite samples. Whereas our samples were
504 produced by simple exchange of Na-birnessite in neutral CaCl_2 solutions, Drits et al. (1998)
505 exchanged Na-buserite in $\text{Ca}(\text{NO}_3)_2$ solutions without controlling pH, which typically attained
506 values of 9 to 10 in their experiments.

507 By contrast, Ca-birnessite samples generated from the reaction of triclinic Na-birnessite
508 at pH 2 with either 0.1 or 1 M CaCl_2 produced selected area electron diffraction patterns that
509 typically were free of streaks or superstructure reflections (Fig. 8B). HRTEM images of these
510 crystals (Fig. 8C) likewise showed few microstructural defects, although faint superstructure
511 reflections halfway along the $[100]^*$ and $[010]^*$ directions were sometimes apparent, suggesting
512 doubling of a and b in local areas.

513 We suggest that the superstructure reflections arise from short-range order among the interlayer
514 Ca atoms and water molecules. This assumption is supported by the observation that different
515 interlayer cations result in different patterns of superstructure reflections (Post and Veblen 1990;
516 Drits et al. 1997, 1998; Lopano et al. 2007, 2009). In contrast, hexagonal birnessite structures
517 show faint or no superstructure reflections because most of the interlayer cations are locked into
518 sites above and below octahedral vacancies. Drits et al. (1997) postulate that the superstructures
519 indicate ordering of distorted Mn^{3+} octahedra into rows, such that one row of Mn^{3+} octahedra
520 alternate with two rows of Mn^{4+} octahedra. However, we observed no direct evidence of such
521 ordering, and the energetics of structural strain suggest to us that Mn^{3+} cations will tend not to
522 occupy neighboring octahedra, similar to the distribution of Al^{3+} in silicates described by the Al-
523 avoidance rule (Loewenstein 1954; Post and Burnham 1986). In other words, the energy
524 minimization realized by isolating Mn^{3+} is greater than might be obtained by any strain reduction
525 achieved by aligning Jahn-Teller distortions in rows. Additionally, XRD structure refinements

526 reported for large tunnel structure Mn oxides, such as romanechite, todorokite, and woodruffite
527 (Turner and Post 1988; Post et al. 2003) consistently show that Mn^{3+} preferentially orders into
528 octahedra that are at the edges of the widest octahedral chains (*e.g.*, triple chains, or quadruple
529 chains). But in all cases, charge balance considerations and refined Mn octahedral bond distances
530 show that less than half of the octahedra in any particular chain are occupied by Mn^{3+} , thereby
531 avoiding nearest neighbor Mn^{3+} octahedra (as would be the case in the proposed rows of
532 octahedra). Finally, when considering the total structure energy, one must also consider
533 contributions resulting from interlayer cation charge-charge interactions with the Mn in the
534 octahedral sheets. Although a possible secondary effect, previous structure-energy studies
535 indicate a tendency for the interlayer cations to align with the Mn^{3+} octahedra, producing a three-
536 dimensional configuration with Mn^{3+} and interlayer cations occupying approximately 1/3 of the
537 available sites (Cygan et al. 2012).

538 Drits et al. (1998) concluded that their Ca-birnessite samples were composed of mixtures
539 of various structures consistent with the SAED superstructure reflections, and, in fact, such a
540 model might be correct. The C-1 structure model presented in the current study likely represents
541 the long-range average structure, as does X-ray diffraction data, and yields excellent overall
542 Rietveld refinements for triclinic Ca-birnessite samples exchanged over a range of pH values and
543 Ca concentrations.

544

545 *Comparison of synthetic Ca-birnessite and ranciéite*

546 Ca-rich birnessite-like phases are common in a variety of natural systems (*e.g.*, Tebo et
547 al. 2004; Bargar et al. 2005; Webb et al. 2005; Tan et al. 2010). In most of these cases, it was
548 assumed, or at least suggested, that the Mn oxide phases formed by some type of biologically

549 mediated process involving bacteria, fungi, or similar microorganisms. Additionally, the Ca-
550 analogue to the mineral birnessite, ranciéite, has been found as an abiogenic product in numerous
551 low-temperature alpine vein deposits and in oxidized zones of Fe and Mn deposits (Ertl et al.
552 2005). Apparently, Ca cations either are particularly effective at stabilizing birnessite-like
553 structures, or Ca-rich birnessites are energetically or kinetically favored in natural environments.
554 Furthermore, as mentioned above, ranciéite-like structures play critical roles in water-oxidation
555 catalysis and as the oxygen-evolving complex within the enzyme photosystem II (PSII) (Umena
556 et al. 2011; Zhang et al. 2015; Yamaguchi et al. 2017).

557 Ranciéite ($\text{Ca}_{0.19}\text{K}_{0.01}(\text{Mn}^{4+}_{0.91}\square_{0.09})\text{O}_2 \cdot 0.63 \text{H}_2\text{O}$) has a hexagonal structure (Post et al.
558 2008) that is similar to those of the Ca-birnessites generated when we exchanged Na-birnessite at
559 low pH and low Ca concentrations. In ranciéite, 9% of the octahedra are vacant, in comparison
560 with the 10% vacancy content of the exchanged Ca-birnessite synthesized at pH 2 and 0.01 *M*
561 Ca^{2+} in this study. The Ca:Mn ratio in ranciéite is 0.21, significantly higher than the average
562 values of ~0.05 observed for the hexagonal Ca-birnessites here (Fig. 3). This disparity is
563 explained by the fact that the ranciéite formed in alpine vein deposits revealed no evidence for
564 Mn^{2+} , which we surmise occurs as an interlayer cation in our exchanged Ca-birnessites.

565 In both ranciéite and hexagonal Ca-birnessite produced by exchange, Ca cations occupy
566 positions above and below vacancies in the Mn octahedral sheets. Further, through tridentate
567 coordination with the octahedral O atoms associated with the vacancies and tridentate
568 coordination with water molecules at $z = 0.5$, the Ca^{2+} (and/or Mn^{2+}) cations occupy highly
569 regular octahedral sites within the interlayer (Fig. 1C). Fischer et al. (2018) have argued that the
570 presence of these cations is at least as important as the absence of distortional Mn^{3+} in promoting

571 the *P*-3 symmetry of hexagonal birnessite structures, since selective removal of octahedral Mn³⁺
572 from triclinic birnessite by siderophores induced no symmetry change.

573 Although the Ca-exchanged birnessite structures exchanged above pH 3 were
574 unambiguously triclinic, this study does reinforce the conclusion in Ling et al. (2018) that Ca-
575 birnessites are “less triclinic” – with smaller distortions from hexagonal symmetry – than are
576 Na-, K-, Ba-, and Cs-birnessite. In addition, when the percentages of Mn²⁺ and Mn³⁺ as
577 measured by XPS are compared for different varieties of birnessite, the triclinic birnessites
578 cluster separately from the synthetic and natural hexagonal birnessites (Fig. 10). Moreover, the
579 Ca-birnessites from the present study reside close to the morphotropic phase boundaries (Heaney
580 2000) that separate the triclinic and hexagonal symmetry fields. Thus, triclinic Ca-birnessite is in
581 a sense transitional between hexagonal ranciéite-type birnessites and the other triclinic alkali-
582 and alkaline-earth birnessites. Moreover, in the triclinic Ca-birnessite phases, our refinements
583 indicate that at least some of the Ca²⁺ is disordered with water molecules halfway between the
584 octahedral sheets. Perhaps then, the size and charge of Ca²⁺ confers a flexibility to occupy
585 different interlayer sites equally well, making it a particularly effective partner with Mn to build
586 birnessite- (or ranciéite-) like structures. Moreover, to the extent that Ca²⁺ is equally capable of
587 coordinating with octahedral O atoms alongside Mn²⁺ at *z* = 0.7 or coordinating with water
588 molecules near *z* = 0.5, these results may offer some insights into the mechanism of the CaMn₄
589 oxygen-evolving complex, particularly since Mn redox changes are associated with these
590 different interlayer positions.

591

592 **IMPLICATIONS**

593 Ca-rich phylломanganates occur in a variety of natural systems, and detailed knowledge
594 of their structures is essential to understanding, and modeling, their roles as geochemical agents.
595 The exchange experiments described here, performed over a range of pH values (3 to 7.5) and
596 Ca²⁺ concentrations (0.01 to 1 M) that are relevant to natural environments, yielded Ca-birnessite
597 products that all have the same triclinic structure with nearly identical unit-cell parameters. This
598 observation suggests the existence of a Ca-birnessite structure that is distinct from that of other
599 triclinic birnessite phases with different interlayer cations. Our results also reveal that the
600 transformation of Na- to Ca-birnessite is more than a simple replacement of Na by Ca; in
601 addition to adjustments to the layer stacking configuration to accommodate a different
602 size/charge cation, as evidenced by the changes in unit-cell angles, some of the Mn³⁺ cations in
603 the octahedral layers are reduced to Mn²⁺, which migrates into the interlayer. As various studies
604 have suggested that Mn³⁺, and vacancies, in the octahedral sheets are particularly active sites for
605 cation absorption and/or redox reactions, our work indicates that the identities of interlayer
606 cations affect the Mn oxidation profile and consequently the reactivity of phylломanganates.
607 Additionally, the XPS results show that although the relative amounts of the different Mn
608 oxidation states change for the various Ca-exchanges, the average oxidation states remain the
609 same, indicating that although there is a transfer of electrons within a particular birnessite phase,
610 there is not net change in the overall redox state.

611 Samples produced by Ca-exchange at pH values of 2 and 3 have significantly lower Ca
612 contents than those formed under higher pH conditions, and exhibit hexagonal, or nearly
613 hexagonal, structures, or are mixtures of hexagonal and triclinic phases. The hexagonal structure
614 compares closely with those previously reported for synthetic hexagonal birnessite-like phases
615 and for the mineral ranciéite. We propose that the structures determined here for triclinic Ca-

616 birnessite and hexagonal Ca-birnessite are improved analogues for modeling natural Ca-
617 phyllomanganates. Additionally, the charge and size characteristics of Ca²⁺ perhaps make it
618 particularly suited for forming birnessite/ranciéite-like structures, *e.g.* the oxygen-evolving
619 complex within the enzyme photosystem II (PSII).

620

621 **ACKNOWLEDGMENTS**

622 This research was carried out at National Museum of Natural History, Department of
623 Mineral Sciences, Smithsonian Institution. Scott D. Whittaker is kindly acknowledged for his
624 technical support during the use of FEI Apreo scanning electron microscope at National Museum
625 of Natural History, Smithsonian Institution. Si Athena Chen collected synchrotron X-ray
626 diffraction data at Beamline 13-BM_C at the Advanced Photon Source, Argonne National
627 Laboratory. Ke Wang assisted with transmission electron microscopy in the Materials
628 Characterization Laboratory, Penn State. We also acknowledge NSF EAR-1552211 and the
629 Miller Faculty Fellowship (College of Earth and Mineral Sciences, PSU). This research used
630 resources of the Advanced Photon Source, a U.S. Department of Energy (DOE) Office of
631 Science User Facility operated for the DOE Office of Science by Argonne National Laboratory
632 under Contract No. DE-AC02-06CH11357. ESI was supported by U.S. Department of Energy
633 (DOE), Office of Science, Office of Basic Energy Sciences (BES), Chemical Sciences,
634 Geosciences, and Biosciences Division through its Geosciences program at Pacific Northwest
635 National Laboratory (PNNL). PNNL is a multiprogram national laboratory operated by Battelle
636 Memorial Institute under Contract No. DE-AC05-76RL01830 for the U.S. DOE. A portion of the
637 research was performed using EMSL (grid.436923.9), a DOE Office of Science User Facility
638 sponsored by the Office of Biological and Environmental Research. Four anonymous reviewers

639 are kindly acknowledged for their thoughtful comments and suggestions that significantly
640 improved the manuscript.

641

642 REFERENCES

643

644 Adreiadis, E.S., Chavarot-Kerlidou, M., Fontecave, M., and Artero, V. (2011) Artificial
645 photosynthesis: from molecular catalysts for light-driven water splitting to
646 photoelectrochemical cells. *Photochemistry and Photobiology*, 87(5), 946-64.

647 Bargar, J.R., Fuller, C.C., Marcus, M.A., Brearley, A.J., De la Rosa, M.P., Webb, S.M. and
648 Caldwell, W.A. (2009). Structural characterization of terrestrial microbial Mn oxides from
649 Pinal Creek, AZ. *Geochimica et Cosmochimica Acta*, 73, 889-910.

650 Boumaiza, H., Renard, A., Robinson, M.R., Kervern, G., Vidal, L., Ruby, C., Bergaoui, L., and
651 Coustel, R. (2019) A multi-technique approach for studying Na triclinic and hexagonal
652 birnessites. *Journal of Solid State Chemistry*, 272, 234-243.

653 Chukhrov, F.V., Gorshkov, A.I., Sivtsov, A.V., and Berezovskaya, V.V. (1979) A new 14 Å
654 mineral of the birnessite group in deep-sea micronodules. *Nature*, 280, 136-137.

655 Cui, H., Liu, F., Feng, X., Tan, W., and Wang, M.K. (2010) Aging promotes todorokite
656 formation from layered manganese oxide at near-surface conditions. *Journal of Soils and*
657 *Sediments*, 10(8), 1540-1547.

658 Cygan, R.T., Post, J.E., Heaney, P.J. and Kubicki, J.D. (2012) Molecular models of birnessite
659 and related hydrated layered minerals. *American Mineralogist*, 97, 1505-1514.

660 Drits, V.A., Lanson, B., Gorshkov, A.I., and Manceau, A. (1998) Substructure and superstructure
661 of four-layer Ca-exchanged birnessite. *American Mineralogist*, 83(1-2), 97-118.

- 662 Drits, V.A., Silvester, E., Gorshkov, A.I., and Manceau, A. (1997) Structure of synthetic
663 monoclinic Na-rich birnessite and hexagonal birnessite: I. Results from X-ray diffraction
664 and selected-area electron diffraction. *American Mineralogist*, 82, 946–961.
- 665 Ertl, A., Pertlik, F., Prem, M., Post, J.E., Kim, S.J., Brandstatter, F., and Schuster, R. (2005)
666 Ranciéite crystals from Friesach, Carinthia, Austria. *European Journal of Mineralogy*, 17,
667 163–172.
- 668 Feng, M., Du, Q., Su, L., Zhang, G., Wang, G., Ma, Z., Gao, W., Qin, X., and Shao, G. (2017)
669 Manganese oxide electrode with excellent electrochemical performance for sodium ion
670 batteries by pre-intercalation of K and Na ions. *Nature Scientific Reports*, 7(1), 2219.
- 671 Feng, X.H., Liu, F., Tan, W.F., and Liu, X.W. (2004) Synthesis of Birnessite from the Oxidation
672 of Mn^{2+} by O_2 in Alkali Medium: Effects of Synthesis Conditions. *Clays and Clay*
673 *Minerals*, 52(2), 240-250.
- 674 Feng, X.H., Zhai, L.M., Tan, W.F., Liu, F., and He, J.Z. (2007) Adsorption and redox reactions
675 of heavy metals on synthesized Mn oxide minerals. *Environmental Pollution* 147(2), 366-
676 73.
- 677 Finger, L.W., Cox, D.E., and Jephcoat, A.P. (1994) A correction for powder diffraction peak
678 asymmetry due to axial divergence. *Journal of Applied Crystallography*, 27(6), 892-900.
- 679 Fischel, M.H., Fischel, J.S., Lafferty, B.J., and Sparks, D.L. (2015) The influence of
680 environmental conditions on kinetics of arsenite oxidation by manganese-oxides.
681 *Geochemical Transactions*, 16, 15.
- 682 Fischer, T.B. (2010) Structural Transformations of Birnessite (δ - MnO_2) During Biological and
683 Abiological Reduction. Doctoral dissertation, Pennsylvania State University.

- 684 Fischer, T.B., Heaney, P.J. and Post, J.E. (2018). Changes in the structure of birnessite during
685 siderophore-promoted dissolution: A time-resolved synchrotron X-ray diffraction study.
686 Chemical Geology, 476, 46-58.
- 687 Fleegeer, C.R., Heaney, P.J., and Post, J.E. (2013) A time-resolved X-ray diffraction study of Cs
688 exchange into hexagonal H-birnessite. American Mineralogist, 98, 671-679.
- 689 Frey, C.E., Wiechen, M., and Kurz, P. (2014) Water-oxidation catalysis by synthetic manganese
690 oxides--systematic variations of the calcium birnessite theme. Dalton Transactions, 43(11),
691 4370-9.
- 692 Golden, D.C., Dixon, J.B., and Chen, C.C. (1986) Ion exchange, thermal transformations, and
693 oxidizing properties of birnessite. Clays and Clay Minerals, 34(5), 511-520.
- 694 Grangeon, S., Lanson, B., Miyata, N., Tani, Y. and Manceau, A. (2010). Structure of
695 nanocrystalline phyllo-manganates produced by freshwater fungi. American Mineralogist,
696 95, 1608-1616.
- 697 Händel, M., Rennert, T., and Totsche, K.U. (2013) A simple method to synthesize birnessite at
698 ambient pressure and temperature. Geoderma, 193-194, 117-121.
- 699 Heaney, P.J. (2000). Phase transformations induced by solid solution. Reviews in Mineralogy
700 and Geochemistry, 39, 135-174.
- 701 Hinkle, M.A.G., Flynn, E.D., and Catalano, J.G. (2016) Structural response of phyllo-manganates
702 to wet aging and aqueous Mn(II). Geochimica Et Cosmochimica Acta, 192, 220-234.
- 703 Hou, H.J.M. (2011) Manganese-based Materials Inspired by Photosynthesis for Water-Splitting.
704 Materials 4(10), 1693-1704.
- 705 Housecroft, C.E., and Jenkins, H.D.B. (2017) Absolute ion hydration enthalpies and the role of
706 volume within hydration thermodynamics. Rsc Advances, 7(45), 27881-27894.

- 707 Hsu, Y. K., Chen, Y. C., Lin, Y. G., Chen, L. C., & Chen, K. H. (2011). Reversible phase
708 transformation of MnO₂ nanosheets in an electrochemical capacitor investigated by in situ
709 Raman spectroscopy. *Chemical Communications*, 47, 1252-1254.
- 710 Huang, M., Zhang, Y., Li, F., Zhang, L., Ruoff, R.S., Wen, Z., and Liu, Q. (2014) Self-assembly
711 of mesoporous nanotubes assembled from interwoven ultrathin birnessite-type MnO₂
712 nanosheets for asymmetric supercapacitors. *Nature Scientific Reports*, 4, 3878.
- 713 Ilton, E.S., Post, J.E., Heaney, P.J., Ling, F.T. and Kerisit, S.N. (2016) XPS determination of Mn
714 oxidation states in Mn (hydr) oxides. *Applied Surface Science*, 366, 475-485.
- 715 Iyer, A., Del-Pilar, J., King'ondo, C.K., Kissel, E., Garces, H.F., Huang, H., El-Sawy, A.M.,
716 Dutta, P.K., and Suib, S.L. (2012) Water Oxidation Catalysis using Amorphous
717 Manganese Oxides, Octahedral Molecular Sieves (OMS-2), and Octahedral Layered (OL-
718 1) Manganese Oxide Structures. *Journal of Physical Chemistry C*, 116(10), 6474-6483.
- 719 Jiao, F., and Frei, H. (2010) Nanostructured manganese oxide clusters supported on mesoporous
720 silica as efficient oxygen-evolving catalysts. *Chemical Communications*, 46(17), 2920-2.
- 721 Johnson, E.A., and Post, J.E. (2006) Water in the interlayer region of birnessite: Importance in
722 cation exchange and structural stability. *American Mineralogist*, 91(4), 609-618.
- 723 Jones, L.H.P., and Milne, A.A. (1956) Birnessite, a new manganese oxide mineral from
724 Aberdeenshire, Scotland. *Mineralogical Magazine*, 31, 283-288.
- 725 Julien, C. (2003) Raman spectra of birnessite manganese dioxides. *Solid State Ionics*, 159(3-4),
726 345-356.
- 727 Julien, C.M., Massot, M., and Poinسیون, C. (2004) Lattice vibrations of manganese oxides.
728 *Spectrochimica Acta Part A: Molecular and Biomolecular Spectroscopy*, 60(3), 689-700.

- 729 Kim, S.J. (1980) Birnessite and ranciete problem; their crystal chemistry and new classification.
730 Journal of the Geological Society of Korea, 16, 105–113.
- 731 Kim, S.J. (1991) New characterization of takanelite. American Mineralogist, 76, 1426-1430.
- 732 Kong, Kyeong Pil (2017) Mineralogical and geochemical constraints of chromium oxidation
733 induced by birnessite. Master's Thesis, Pennsylvania State University.
- 734 Kuma, K., Usui, A., Paplawsky, W., Gedulin, B., and Arrhenius, G. (1994) Crystal Structures of
735 Synthetic 7 Å and 10 Å Manganates Substituted by Mono- and Divalent Cations.
736 Mineralogical Magazine, 58, 425-447.
- 737 Kwon, K.D., Refson, K., and Sposito, G. (2013) Understanding the trends in transition metal
738 sorption by vacancy sites in birnessite. Geochimica Et Cosmochimica Acta, 101, 222-232.
- 739 Landrot, G., Ginder-Vogel, M., Livi, K., Fitts, J.P., and Sparks, D.L. (2012) Chromium(III)
740 oxidation by three poorly crystalline manganese(IV) oxides. 2. Solid phase analyses.
741 Environmental Science & Technology, 46(21), 11601-9.
- 742 Lanson, B., Drits, V.A., Silvester, E., and Manceau, A. (2000) Structure of H-exchanged
743 hexagonal birnessite and its mechanism of formation from Na-rich monoclinic busserite at
744 low pH. American Mineralogist, 85, 826–838.
- 745 Le Goff, P., Baffier, N., Bach, S., and Pereira-Ramos, J.P. (1996) Synthesis, ion exchange and
746 electrochemical properties of lamellar phyllomanganates of the birnessite group. Materials
747 Research Bulletin, 31(1), 63-75.
- 748 Leinenweber, K. (2005) Welcome to the Crystal Cracker program page, by Kurt Leinenweber.
749 http://multianvil.asu.edu/Crystal_Cracker/CrystalCracker.html (accessed March 19, 2019)

- 750 Lefkowitz, J.P., Rouff, A.A., and Elzinga, E.J. (2013) Influence of pH on the reductive
751 transformation of birnessite by aqueous Mn(II). *Environmental Science & Technology*,
752 47(18), 10364-71.
- 753 Ling, F.T., Heaney, P.J., Post, J.E., and Gao, X. (2015) Transformations from triclinic to
754 hexagonal birnessite at circumneutral pH induced through pH control by common
755 biological buffers. *Chemical Geology*, 416, 1-10.
- 756 Ling, F.T., Post, J.E., Heaney, P.J., and Ilton, E.S. (2018) The relationship between Mn oxidation
757 state and structure in triclinic and hexagonal birnessites. *Chemical Geology*, 479, 216-227.
- 758 Ling, F.T., Post, J.E., Heaney, P.J., Kubicki, J.D., and Santelli, C.M. (2017) Fourier-transform
759 infrared spectroscopy (FTIR) analysis of triclinic and hexagonal birnessites.
760 *Spectrochimica Acta Part A: Molecular and Biomolecular Spectroscopy*, 178, 32-46.
- 761 Loewenstein, W. (1954) The distribution of aluminum in the tetrahedra of silicates and
762 aluminates. *American Mineralogist*, 39, 92-96.
- 763 Lopano, C.L., Heaney, P.J., Post, J.E., Hanson, J., and Komarneni, S. (2007) Time-resolved
764 structural analysis of K- and Ba-exchange reactions with synthetic Na-birnessite using
765 synchrotron X-ray diffraction. *American Mineralogist*, 92(2-3), 380-387.
- 766 Lopano, C.L., Heaney, P.J., Bandstra, J.Z., Post, J.E., and Brantley, S.L. (2011) Kinetic analysis
767 of cation exchange in birnessite using time-resolved synchrotron X-ray diffraction.
768 *Geochimica et Cosmochimica Acta*, 75, 3973-3981.
- 769 Lopano, C.L., Heaney, P.J. and Post, J.E. (2009) Cs-exchange in birnessite: Reaction
770 mechanisms inferred from time-resolved X-ray diffraction and transmission electron
771 microscopy. *American Mineralogist*, 94, 816-826.

- 772 Manceau, A., Lanson, B., and Drits, V.A. (2002) Structure of heavy metal sorbed birnessite. Part
773 III: Results from powder and polarized extended X-ray absorption fine structure
774 spectroscopy. *Geochimica Et Cosmochimica Acta*, 66(15), 2639-2663.
- 775 Manning, B.A., Fendorf, S.E., Bostick, B., and Suarez, D.L. (2002) Arsenic(III) oxidation and
776 arsenic(V) adsorption reactions on synthetic birnessite. *Environmental Science &*
777 *Technology*, 36(5), 976-81.
- 778 McKenzie, R.M. (1971) The Synthesis of Birnessite, Cryptomelane, and Some Other Oxides and
779 Hydroxides of Manganese. *Mineralogical Magazine*, 38(296), 493-502.
- 780 McKeown, D.A., and Post, J.E. (2001) Characterization of manganese oxide mineralogy in rock
781 varnish and dendrites using X-ray absorption spectroscopy. *American Mineralogist*, 86,
782 701-713.
- 783 Najafpour, M.M., Salimi, S., Madadkhani, S., Holynska, M., Tomo, T., and Allakhverdiev, S.I.
784 (2016) Nanostructured manganese oxide on silica aerogel: a new catalyst toward water
785 oxidation. *Photosynthesis Research*, 130(1-3), 225-235.
- 786 Najafpour, M.M., Sedigh, D.J., Pashaei, B., and Nayeri, S. (2013) Water oxidation by nano-
787 layered manganese oxides in the presence of cerium(IV) ammonium nitrate: important
788 factors and a proposed self-repair mechanism. *New Journal of Chemistry*, 37(8), 2448-
789 2459.
- 790 Nambu, M. and Tanida, K. (1971) New mineral takanelite. *The Journal of the Japanese*
791 *Association of Mineralogists, Petrologists and Economic Geologists*, 65, 1-5.
- 792 Post, J.E. (1999) Manganese oxide minerals: crystal structures and economic and environmental
793 significance. *Proceedings of the National Academy of Sciences of the United States of*
794 *America*, 96(7), 3447-54.

- 795 Post, J.E. and Burnham, C.W. (1986) Ionic modeling of mineral structures and energies in the
796 electron gas approximation: TiO₂ polymorphs, quartz, forsterite, diopside. American
797 Mineralogist, 71, 142-150.
- 798 Post, J.E., Heaney, P.J., Cahill, C.L., and Finger, L.W. (2003) Woodruffite: A new Mn oxide
799 structure with 3 x 4 tunnels. American Mineralogist, 88, 1697-1702.
- 800 Post, J.E., Heaney, P.J., and Ertl, A. (2008) Rietveld refinement of the ranciéite structure using
801 synchrotron powder diffraction data. Powder Diffraction, 23(01), 10-14.
- 802 Post, J.E., Heaney, P.J., and Hanson, J. (2002) Rietveld refinement of a triclinic structure for
803 synthetic Na-birnessite using synchrotron powder diffraction data. Powder Diffraction,
804 17(3), 218-221.
- 805 Post, J.E., Heaney, P.J., and Hanson, J. (2003) Synchrotron X-ray diffraction study of the
806 structure and dehydration behavior of todorokite. American Mineralogist, 88, 142-150.
- 807 Post, J.E., and Veblen, D.R. (1990) Crystal structure determinations of synthetic sodium,
808 magnesium, and potassium birnessite using TEM and the Rietveld method. American
809 Mineralogist, 75, 477-489.
- 810 Prescher, C. and Prakapenka, V.B. (2015) DIOPTAS: A program for reduction of two-
811 dimensional X-ray diffraction data and data exploration. High Pressure Research, 35, 223–
812 230.
- 813 Rietveld, H.M. (1969) A Profile Refinement Method for Nuclear and Magnetic Structures.
814 Journal of Applied Crystallography, 2(2), 65-71.
- 815 Santelli, C.M., Webb, S.M., Dohnalkova, A.C. and Hansel, C.M. (2011). Diversity of Mn oxides
816 produced by Mn (II)-oxidizing fungi. Geochimica et Cosmochimica Acta, 75, 2762-2776.

- 817 Sauer, K., and Yachandra, V.K. (2002) A possible evolutionary origin for the Mn₄ cluster of the
818 photosynthetic water oxidation complex from natural MnO₂ precipitates in the early ocean.
819 Proceedings of the National Academy of Sciences, 99(13), 8631-6.
- 820 Shannon, R.D. (1976) Revised Effective Ionic Radii and Systematic Studies of Interatomic
821 Distances in Halides and Chalcogenides. Acta crystallographica. Section A, Foundations of
822 crystallography 32, 751-767.
- 823 Shannon, R.D., Gumerman, P.S., and Chenavas, J. (1975) Effect of octahedral Distortion on
824 Mean Mn³⁺-O Distance. American Mineralogist, 60, 714-716.
- 825 Shumlas, S.L., Singireddy, S., Thenuwara, A.C., Attanayake, N.H., Reeder, R.J., and Strongin,
826 D.R. (2016) Oxidation of arsenite to arsenate on birnessite in the presence of light.
827 Geochemical Transactions, 17, 5.
- 828 Silvester, E., Manceau, A., and Drits, V.A. (1997) Structure of synthetic monoclinic Na-rich
829 birnessite and hexagonal birnessite: II. Results from chemical studies and EXAFS
830 spectroscopy. American Mineralogist, 82, 962-978.
- 831 Smith, D.W. (1977) Ionic Hydration Enthalpies. Journal of Chemical Education, 54(9), 540-542.
- 832 Stephens, P. (1999) Phenomenological model of anisotropic peak broadening in powder
833 diffraction. Journal of Applied Crystallography, 32(2), 281-289.
- 834 Tan, H., Zhang, G.X., Heaney, P.J., Webb, S.M., and Burgos, W.D. (2010) Characterization of
835 manganese oxide precipitates from Appalachian coal mine drainage treatment systems.
836 Applied Geochemistry, 25(3), 389-399.
- 837 Tan, W.F., Lu, S.J., Liu, F., Feng, X.H., He, J.Z., and Koopall, L.K. (2008) Determination of the
838 point-of-zero, charge of manganese oxides with different methods including an improved
839 salt titration method. Soil Science, 173(4), 277-286.

- 840 Tebo, B.M., Bargar, J.R., Clement, B.G., Dick, G.J., Murray, K.J., Parker, D., Verity, R., and
841 Webb, S. M. (2004). Biogenic manganese oxides: properties and mechanisms of formation.
842 Annual Reviews in Earth and Planetary Science, 32, 287-328.
- 843 Thompson, P., Cox, D.E., and Hastings, J.B. (1987) Rietveld refinement of Debye-Scherrer
844 synchrotron X-ray data from Al₂O₃. Journal of Applied Crystallography, 20(2), 79-83.
- 845 Toby, B.H., and Von Dreele, R.B. (2013) GSAS-II: the genesis of a modern open-source all
846 purpose crystallography software package. Journal of Applied Crystallography, 46(2), 544-
847 549.
- 848 Tu, S., Racz, G.J., and Goh, T.B. (1994) Transformations of Synthetic Birnessite as Affected by
849 pH and Manganese Concentration. Clays and Clay Minerals, 42(3), 321-330.
- 850 Turner, S. and Post, J.E. (1988) Refinement of the substructure and superstructure of
851 romanechite. American Mineralogist, 73, 1155-1161
- 852 Umena, Y., Kawakami, K., Shen, J. R. and Kamiya, N. (2011). Crystal structure of oxygen-
853 evolving photosystem II at a resolution of 1.9 Å. Nature, 473, 55-60.
- 854 Wang, M.X., Wang, Y.P., Tan, W.F., Liu, F., Feng, X.H., and Koopal, L.K. (2010) Effect of 1-1
855 electrolyte concentration on the adsorption/desorption of copper ion on synthetic birnessite.
856 Journal of Soils and Sediments, 10(5), 879-885.
- 857 Wang, Y., Feng, X.H., Villalobos, M., Tan, W.F., and Liu, F. (2012) Sorption behavior of heavy
858 metals on birnessite: Relationship with its Mn average oxidation state and implications for
859 types of sorption sites. Chemical Geology, 292, 25-34.
- 860 Webb, S.M., Tebo, B.M. and Bargar, J.R. (2005). Structural characterization of biogenic Mn
861 oxides produced in seawater by the marine Bacillus sp. strain SG-1. American
862 Mineralogist, 90, 1342-1357.

- 863 Wiechen, M., Zaharieva, I., Dau, H., and Kurz, P. (2012) Layered manganese oxides for water-
864 oxidation: alkaline earth cations influence catalytic activity in a photosystem II-like
865 fashion. *Chemical Science*, 3(7), 2330-2339.
- 866 Wiechen, M., Najafpour, M.M., Allakhverdiev, S.I. and Spiccia, L. (2014) Water oxidation
867 catalysis by manganese oxides: learning from evolution. *Energy & Environmental Science*,
868 7, 2203-2212.
- 869 Witzke, T., Pöllmann, H., Gardolinski, J.E.F.C. and Sommariva, M. (2017) Lagalyite, IMA 2016,
870 106.
- 871 Yamaguchi, K., Shoji, M., Isobe, H., Yamanaka, S., Umena, Y., Kawakami, K. and Kamiya, N.
872 (2017) On the guiding principles for understanding of geometrical structures of the
873 CaMn_4O_5 cluster in oxygen-evolving complex of photosystem II. Proposal of estimation
874 formula of structural deformations via the Jahn–Teller effects. *Molecular Physics*, 115,
875 636-666.
- 876 Yang, L.F., Cheng, S., Ji, X., Jiang, Y., Zhou, J., and Liu, M.L. (2015) Investigations into the
877 origin of pseudocapacitive behavior of Mn_3O_4 electrodes using in operando Raman
878 spectroscopy. *Journal of Materials Chemistry A*, 3(14), 7338-7344.
- 879 Yin, H., Liu, F., Feng, X., Hu, T., Zheng, L., Qiu, G., Koopal, L.K., and Tan, W. (2013) Effects
880 of Fe doping on the structures and properties of hexagonal birnessites – Comparison with
881 Co and Ni doping. *Geochimica et Cosmochimica Acta*, 117, 1-15.
- 882 Zaharieva, I., Gonzalez-Flores, D., Asfari, B., Pasquini, C., Mohammadi, M.R., Klingan, K.,
883 Zizak, I., Loos, S., Chernev, P. and Dau, H. (2016). Water oxidation catalysis—role of
884 redox and structural dynamics in biological photosynthesis and inorganic manganese
885 oxides. *Energy & Environmental Science*, 9, 2433-2443.

Revision 4

- 886 Zhang, C., Chen, C., Dong, H., Shen, J. R., Dau, H. and Zhao, J. (2015) A synthetic Mn₄Ca-
887 cluster mimicking the oxygen-evolving center of photosynthesis. *Science*, 348, 690-693.
- 888 Zhao, H., Zhu, M., Li, W., Elzinga, E.J., Villalobos, M., Liu, F., Zhang, J., Feng, X., and Sparks,
889 D.L. (2016) Redox Reactions between Mn(II) and Hexagonal Birnessite Change Its Layer
890 Symmetry. *Environmental Science & Technology*, 50(4), 1750-8.
- 891
- 892

893 **FIGURE CAPTIONS**

894 **Figure 1.** Structure drawings showing a) triclinic Na-birnessite, b) triclinic Ca-birnessite – pH
895 7.5 and 1 M Ca²⁺, and c) hexagonal Ca-exchanged birnessite – pH 2 and 0.01 M Ca²⁺. Magenta
896 atoms - Mn; red atoms - O; yellow atoms – Na/H₂O; purple atoms – Ca/H₂O; blue atoms –
897 Mn²⁺/Ca²⁺.

898 **Figure 2.** Scanning Electron microscopy (SEM) image of Ca-birnessite.

899 **Figure 3.** Graph reporting Ca/Mn ratio in Ca-birnessite structures prepared at different
900 conditions of pH and Ca²⁺ concentration. Asterisk = Ca birn 1M (5min); Green diamond = Ca
901 birn 1M; blue triangle = Ca birn 0.1M; yellow circle= Ca birn 0.1M+DI water; red square = Ca
902 birn 0.01M.

903 **Figure 4.** X-ray diffraction (XRD) patterns for Ca-birnessite samples exchanged with 1 M CaCl₂
904 ·2H₂O solutions.

905 **Figure 5.** Rietveld refinement fits and difference curve for a) triclinic Ca-birnessite exchanged at
906 pH 7.5 and 0.1M Ca²⁺, and b) hexagonal birnessite exchanged at pH 2 and 0.01M Ca²⁺.
907 Observed pattern: blue crosses, calculated pattern: solid green line, and difference between the
908 observed and calculated patterns pattern: aquamarine line.

909 **Figure 6.** Fourier transform infrared spectroscopy (FT-IR) spectra collected in the Mn-O bond
910 vibration range for Ca-birnessite prepared with CaCl₂ ·2H₂O solutions (a) initially at near-neutral
911 pH; (b) initially at pH 3; (c) initially at pH 2.

912 **Figure 7.** Raman spectra of Ca-birnessite synthesized in this study.

913 **Figure 8.** (A) Bright-field TEM image of Ca-birnessite exchanged using 0.1 M CaCl₂ solution at
914 pH 2. (B) Selected area electron diffraction pattern along [001] shows no streaking or

Revision 4

915 superstructures, consistent with space group $P\bar{3}$. C) A high-resolution image of Ca-birnessite
916 (ZA [001]) exchanged at pH 2 with 0.1 M CaCl₂ solution with fast-Fourier transform (FFT,
917 inset). Very weak superperiodic reflections are evident halfway along [100]* and [010]*.

918 **Figure 9.** (A) Bright-field TEM image of a crystal formed from Na-birnessite exchanged with
919 0.1 M CaCl₂ solution at pH 7.5. Dark and light surface striations are typical of these crystals,
920 with a ~59° angle between striations. (B) SAED patterns were best indexed to triclinic $C\bar{1}$ cell,
921 and superperiodic reflections at $1/3 [200]^*$ were apparent. C) An HRTEM image of Ca-birnessite
922 synthesized from triclinic Na-birnessite at pH 7.5 and 0.1 M CaCl₂ solution with FFT of whole
923 image (inset). Lattice fringes are continuous across striation boundaries.

924 **Figure 10.** Percentage of Mn(III) and of Mn(II) relative to the total Mn as determined by X-ray
925 photoelectron spectroscopy. Hashed lines represent morphotropic phase boundaries that separate
926 triclinic from hexagonal birnessites. Data from Ilton et al. (2016) and this study.

927 **Table 1a.** Rietveld refinement results of unit cell parameters for Ca-exchanged birnessite

pH	Ca ²⁺ (M)	Time	a (Å)	b (Å)	c (Å)	α (°)	β (°)	γ (°)
7.5*	0.1	1 day	5.113(1)	2.828(1)	7.009(1)	94.90(1)	89.94(1)	89.55(1)
7.5*	0.01	1 day	5.136(2)	2.832(1)	7.047(3)	94.73(2)	90.27(3)	89.77(2)
6.5	1.0	2 min	5.137(1)	2.828(1)	7.009(1)	94.93(1)	90.48(1)	89.78(1)
6.5	1.0	20 days	5.135(1)	2.826(1)	7.043(1)	94.80(1)	90.40(1)	89.77(1)
5.5	1.0	1 day	5.136(1)	2.826(1)	7.035(1)	95.01(1)	90.40(1)	89.79(1)
4.0	1.0	1 day	5.135(1)	2.825(1)	7.045(1)	94.97(1)	90.49(1)	89.84(1)
3.0	1.0	1 day	5.139(1)	2.829(1)	7.032(1)	94.81(1)	90.43(1)	89.82(1)
3.0 38%	0.1	1 day	5.173(1)	2.845(1)	7.154(1)	95.98(1)	90.64(1)	89.90(1)
62%			2.835(1)		7.258(1)			
3.0 24%	0.01	1 day	5.132(1)	2.809(1)	7.031(1)	95.62(1)	90.67(1)	90.13(1)
76%			2.817(1)		7.139(1)			
2.0*	0.1	1 day	4.919(1)	2.863(1)	7.358(1)	94.25(1)	92.99(1)	90.12(1)
2.0*	0.01	1 day	2.8592(4)		7.368(1)			

928

929 **Table 1b.** Rietveld refinement results of unit cell parameters for Na-birnessite (this study), Hexagonal-birnessite (this study), Li-
 930 birnessite (unpublished results), K-birnessite (Lopano et al. 2007), Ba-birnessite (Lopano et al. 2007), Mg-birnessite (unpublished
 931 results), Cs-birnessite (Lopano et al 2009).

	a (Å)	b (Å)	c (Å)	α (°)	β (°)	γ (°)
Na-birnessite (this study)	5.176(4)	2.848(6)	7.310(3)	89.18(6)	103.26(8)	89.76(4)
Hexagonal-birnessite (this study)	2.820(8)		7.267(5)			
Li-birnessite *	5.1401(4)	2.8424(2)	7.1598(8)	90.04(3)	103.109(8)	90.01(2)
K-birnessite (Lopano et al. 2007)	5.1371(5)	2.8476(2)	7.2129(8)	89.95(1)	100.74(7)	89.704(9)
Ba-birnessite (Lopano et al. 2007)	5.1713(5)	2.8473(9)	7.3039(6)	89.533(8)	102.968(3)	89.903(7)
Mg-birnessite *	5.022(1)	2.842(1)	7.041(2)	89.81(2)	96.11(2)	89.89(2)
Cs-birnessite (Lopano et al 2009)	5.1298(4)	2.8445(6)	7.5029(7)	90.12(3)	101.395(7)	89.958(7)

932 *unpublished result

933

934 **Table 2.** X-ray Photoelectron Spectroscopy (XPS) results.

	Mn⁴⁺ (%)	Mn³⁺ (%)	Mn²⁺ (%)	Average Oxidation State
Ca-birnessite 0.1M pH 7.5	64 (4)	29 (5)	7 (1)	3.57 (3)
Ca-birnessite 0.01M pH 3	67 (4)	22 (9)	11 (5)	3.55 (3)
Ca-birnessite 0.01M pH 2	68 (1)	21 (2)	11 (3)	3.58 (3)

935

936 Note: Errors are 3σ

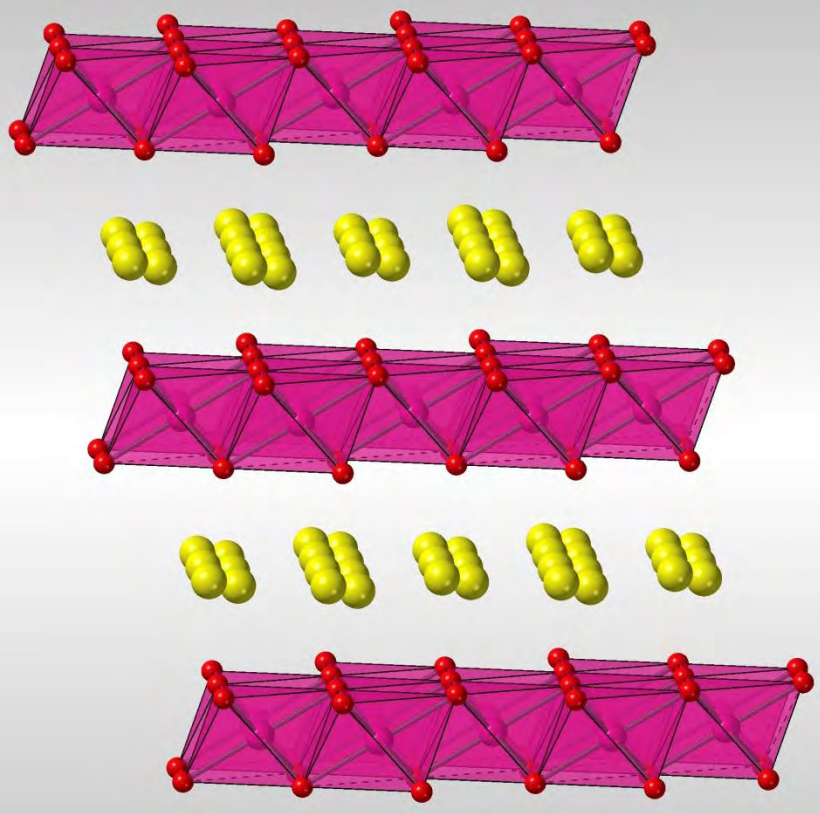


Figure 1a

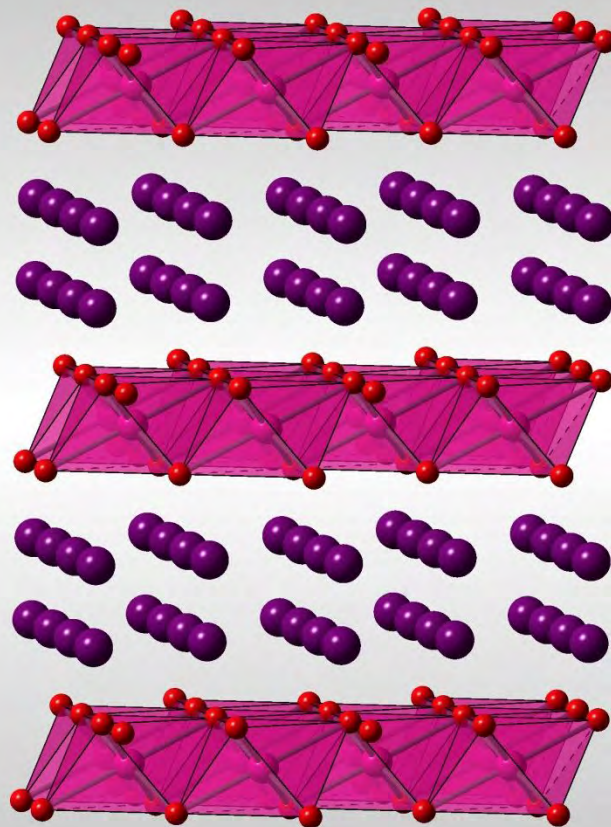


Figure 1b

- Mn2
- MN1
- Ow1
- O1

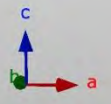
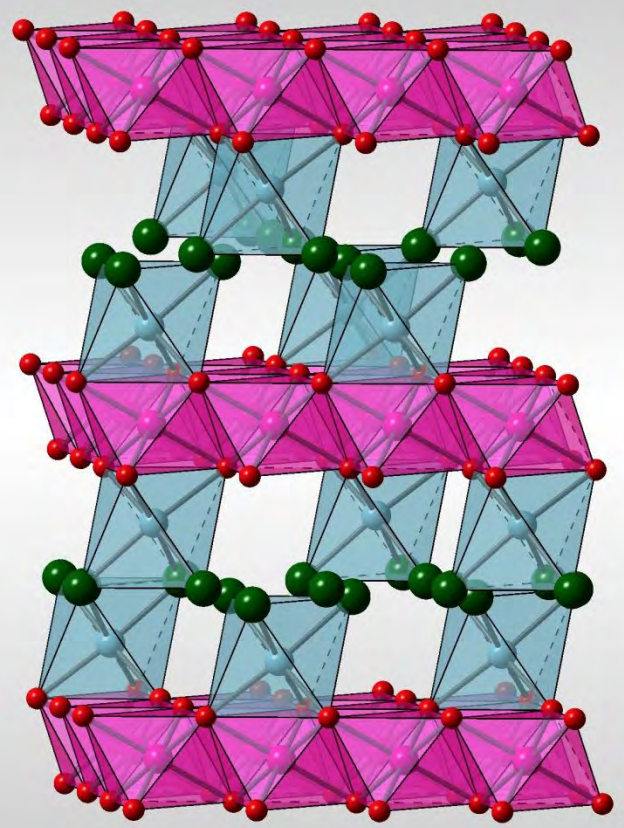


Figure 1c

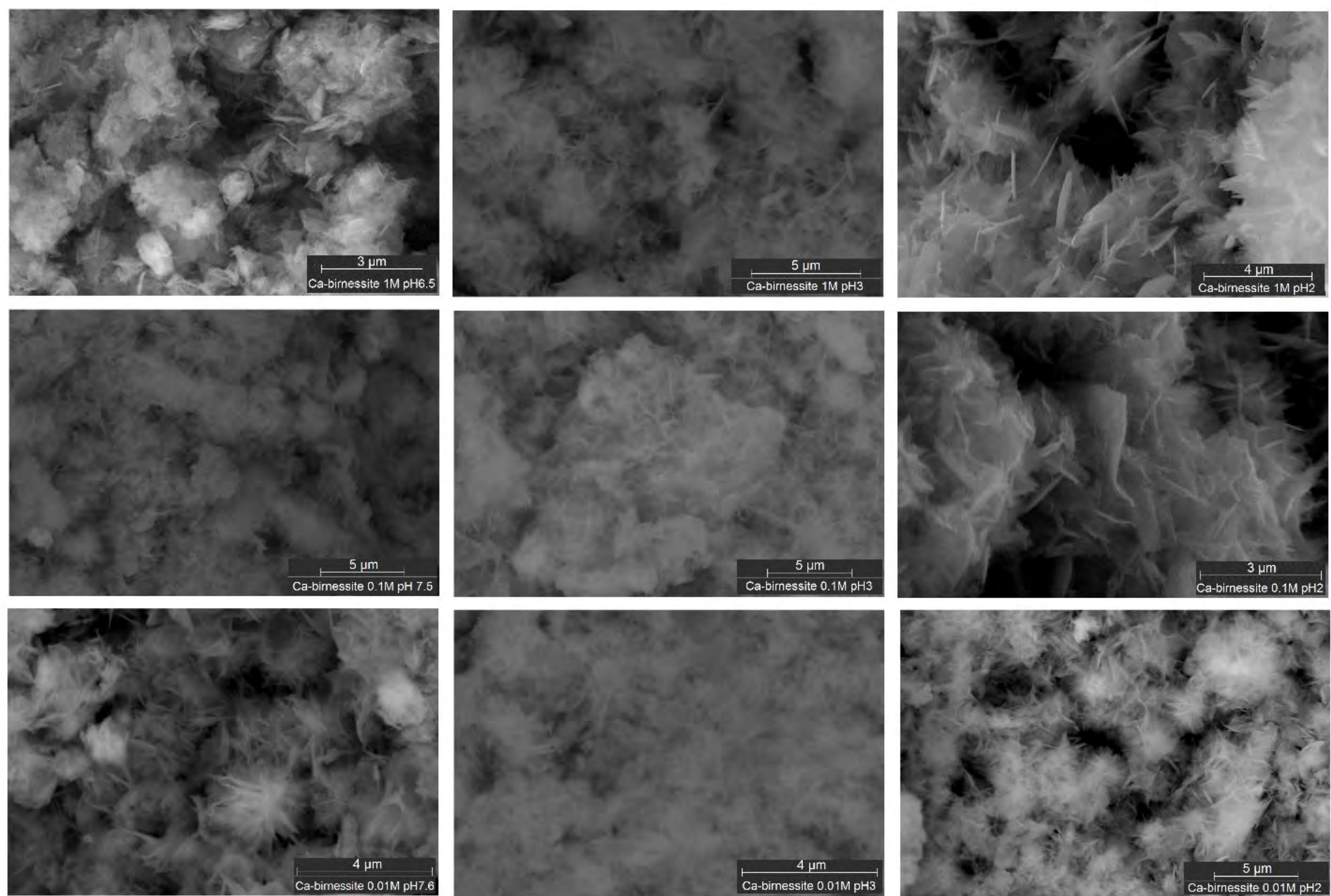


Figure 2

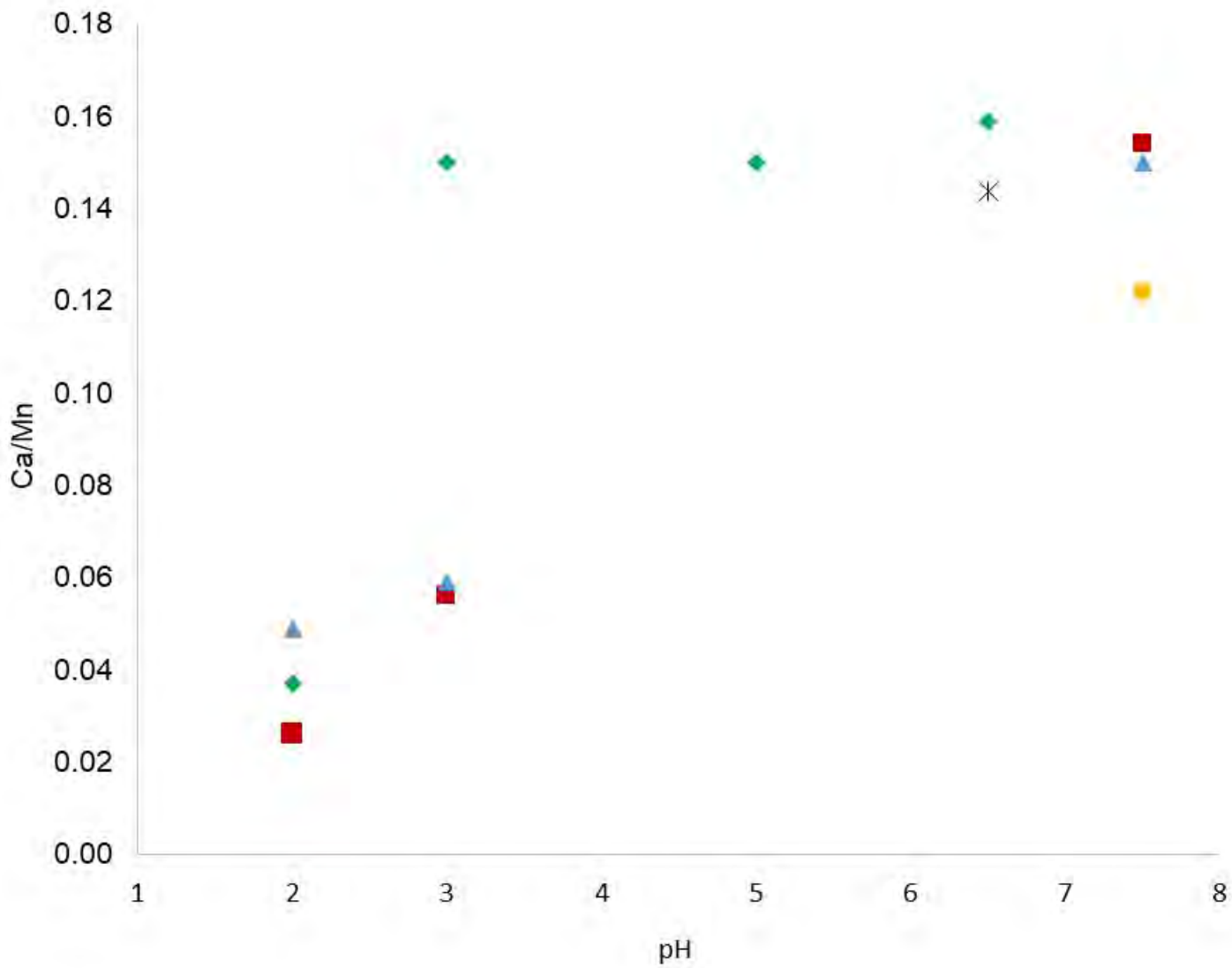


Figure 3

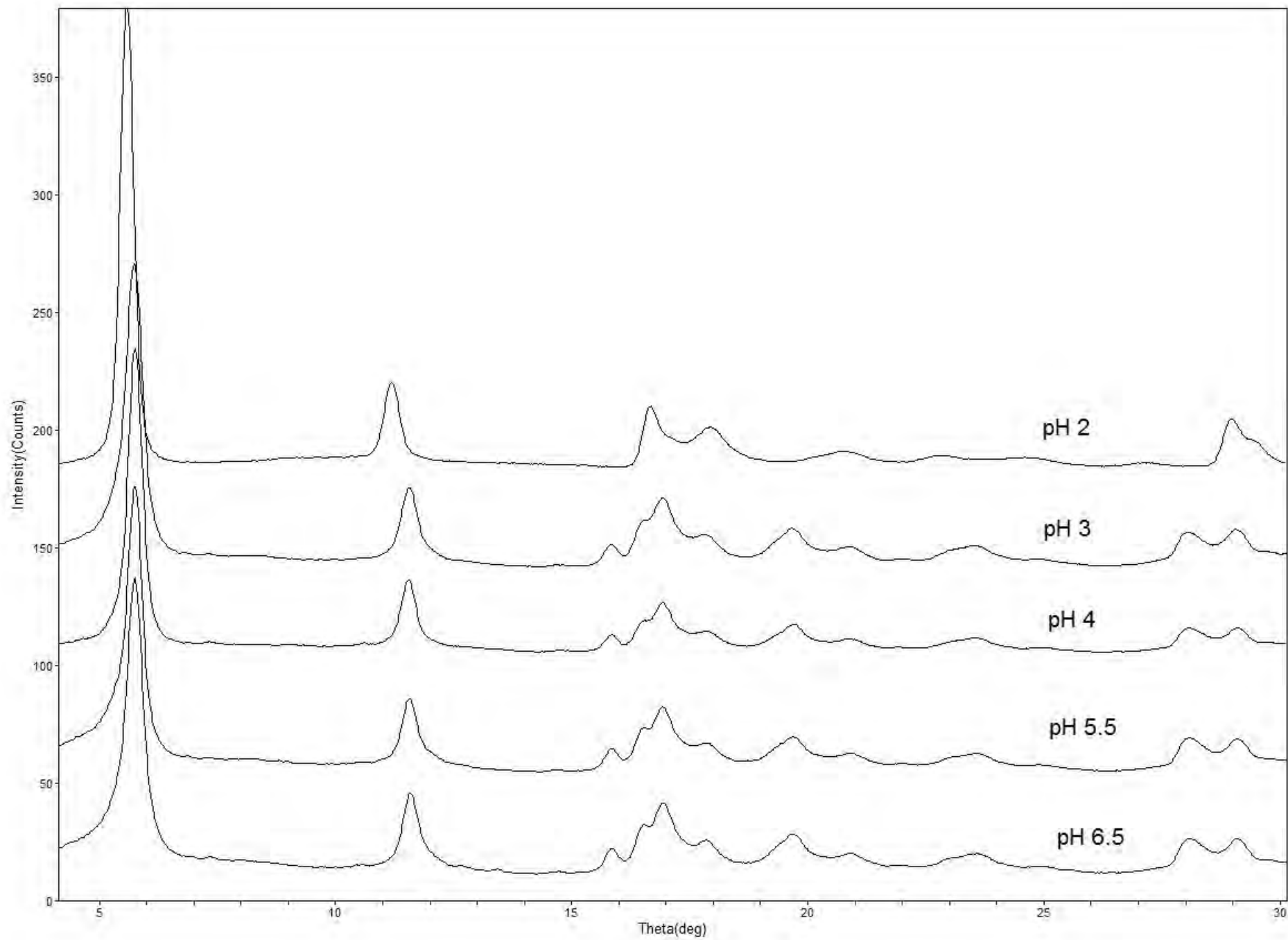


Figure 4

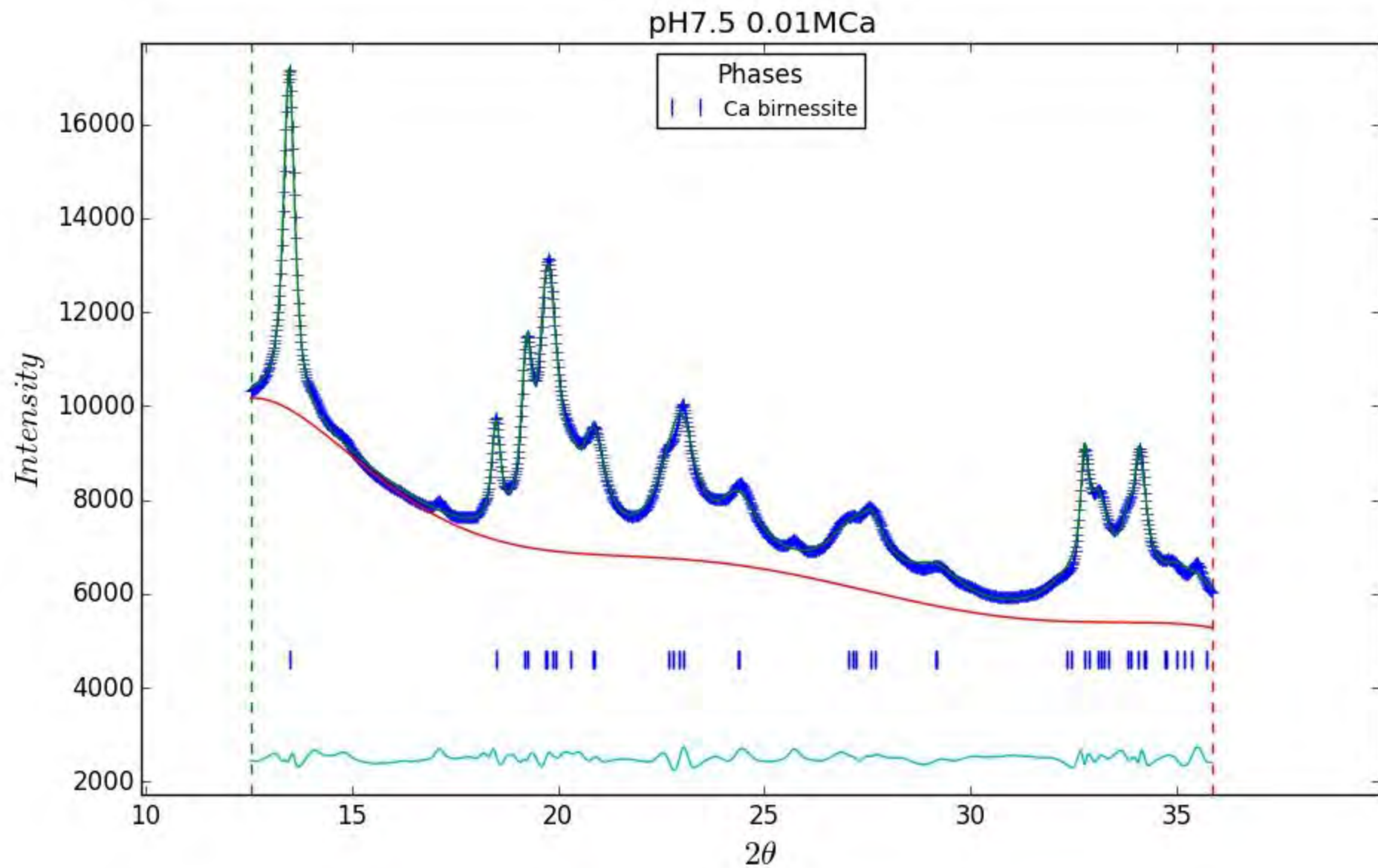


Figure 5a

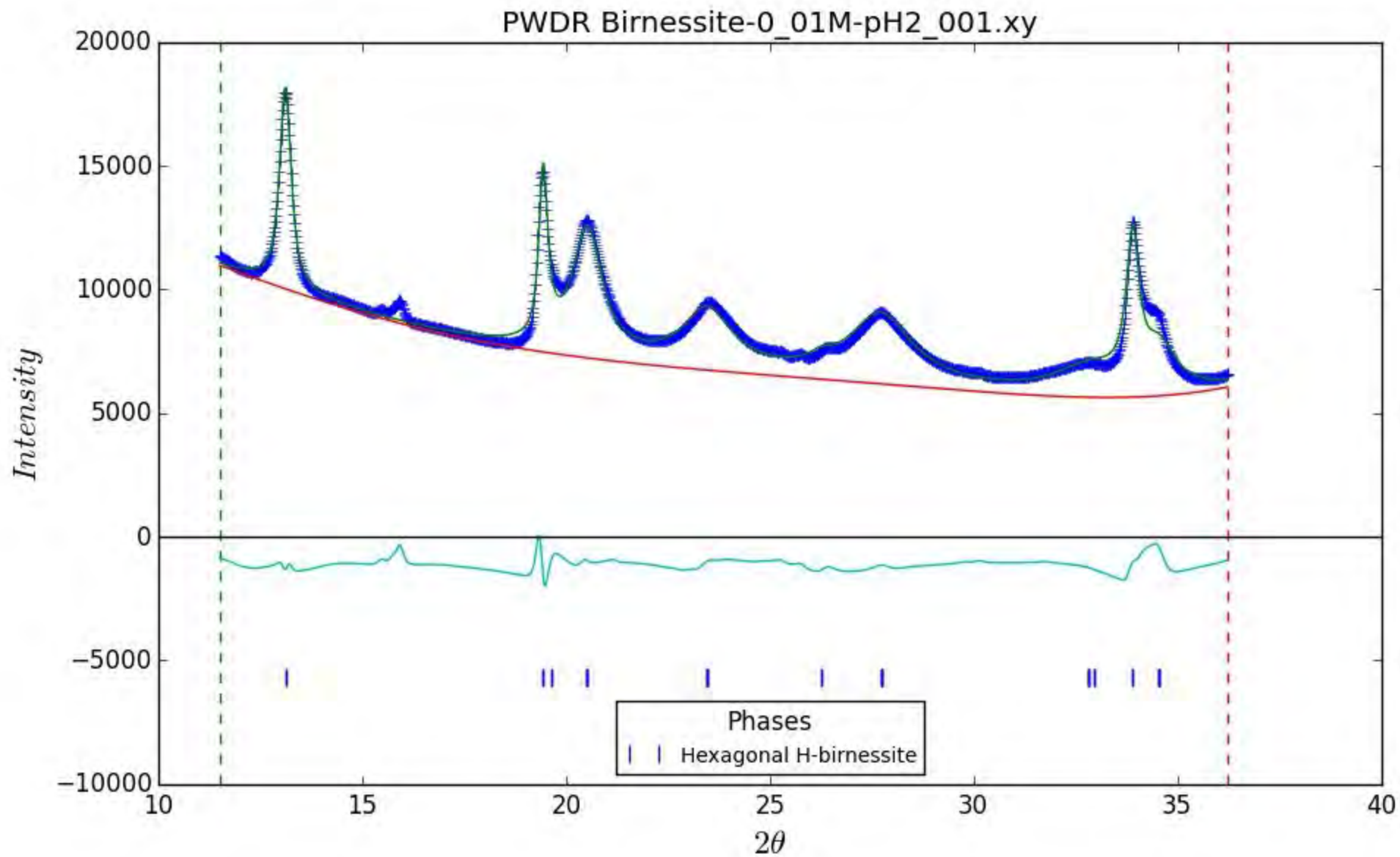


Figure 5b

pH near-neutral

—Na birnessite

—Ca birn 1M pH6.5

—Ca birn 0.1M pH7.5

—Ca birn 0.01M pH7.6

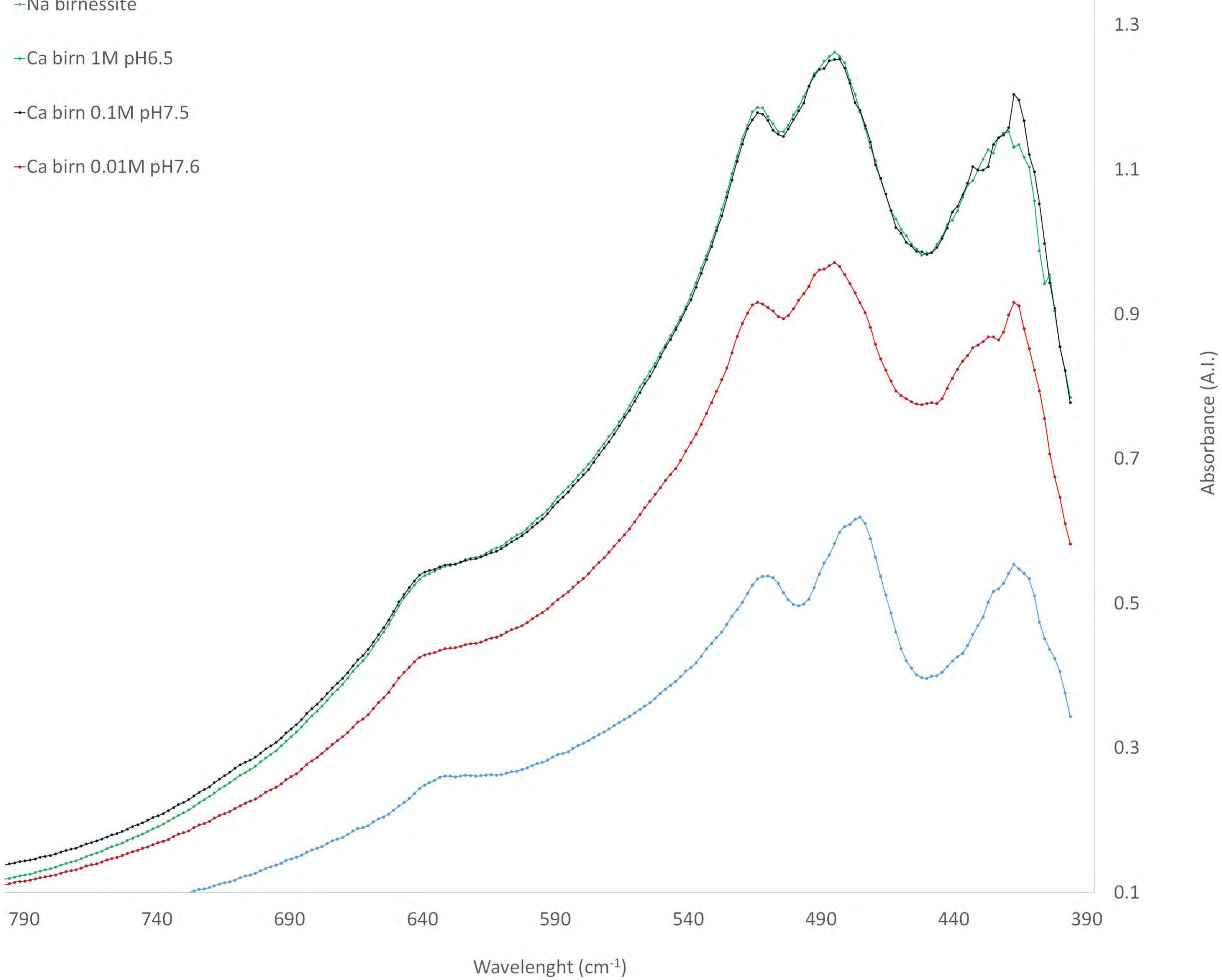


Figure 6a

pH 3

- Na birnessite
- H birnessite
- Ca birn 1M pH3
- Ca birn 0.1M pH3
- Ca birn 0.01M pH3

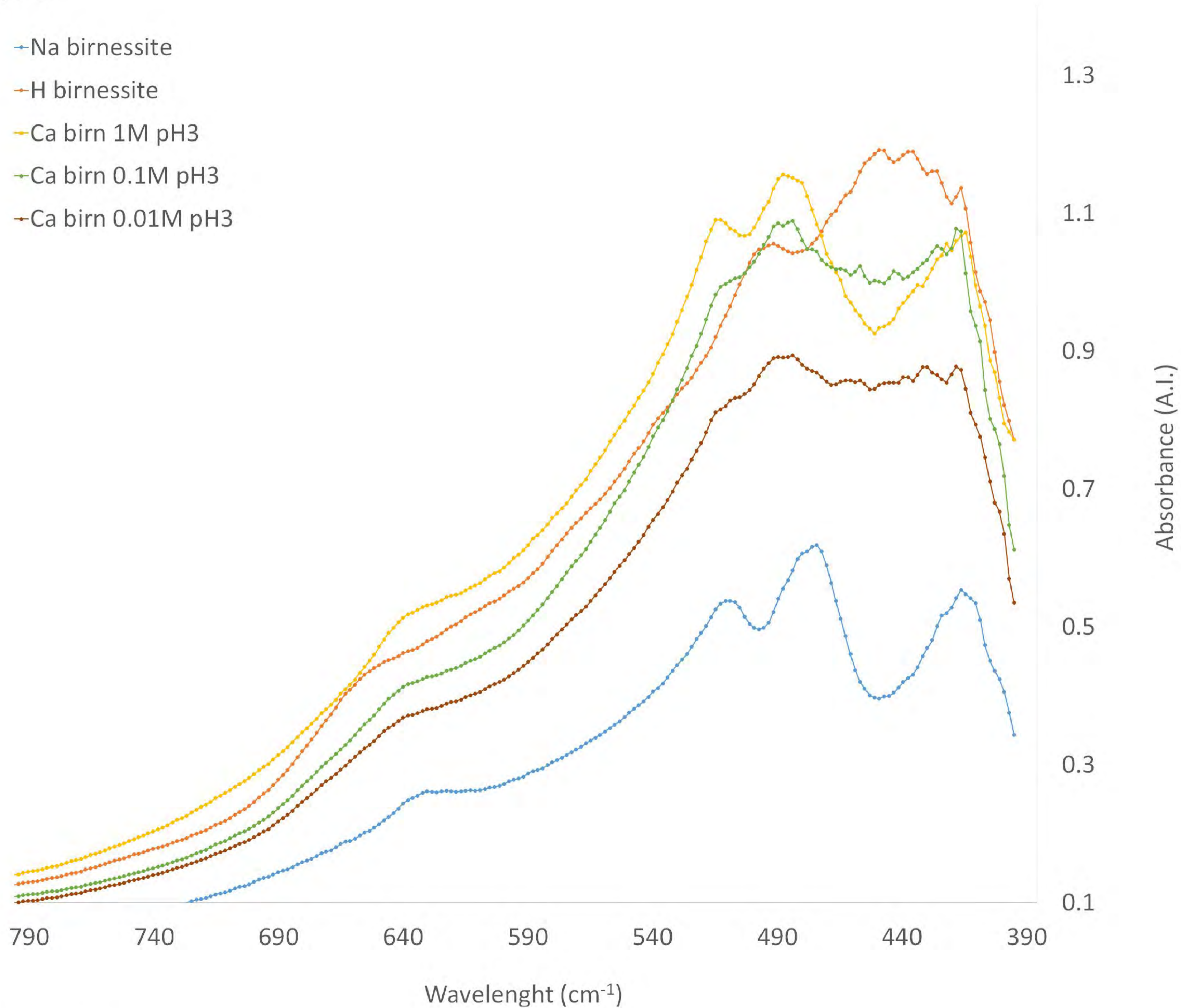


Figure 6b

pH 2

Na birnessite

H birnessite

Ca-birn 1M pH2

Ca birn 0.1M pH 2

Ca birn 0.01 M pH 2

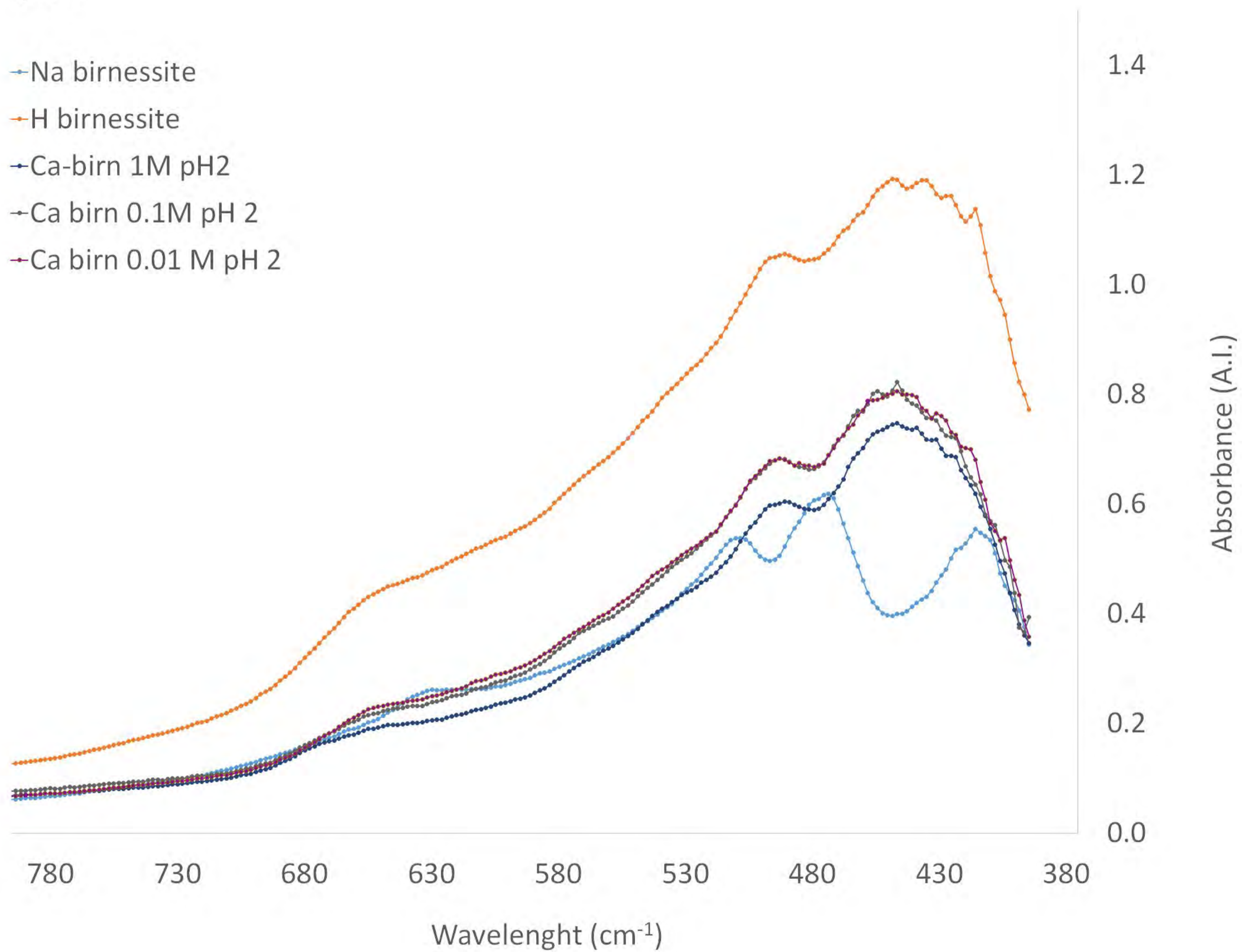


Figure 6c

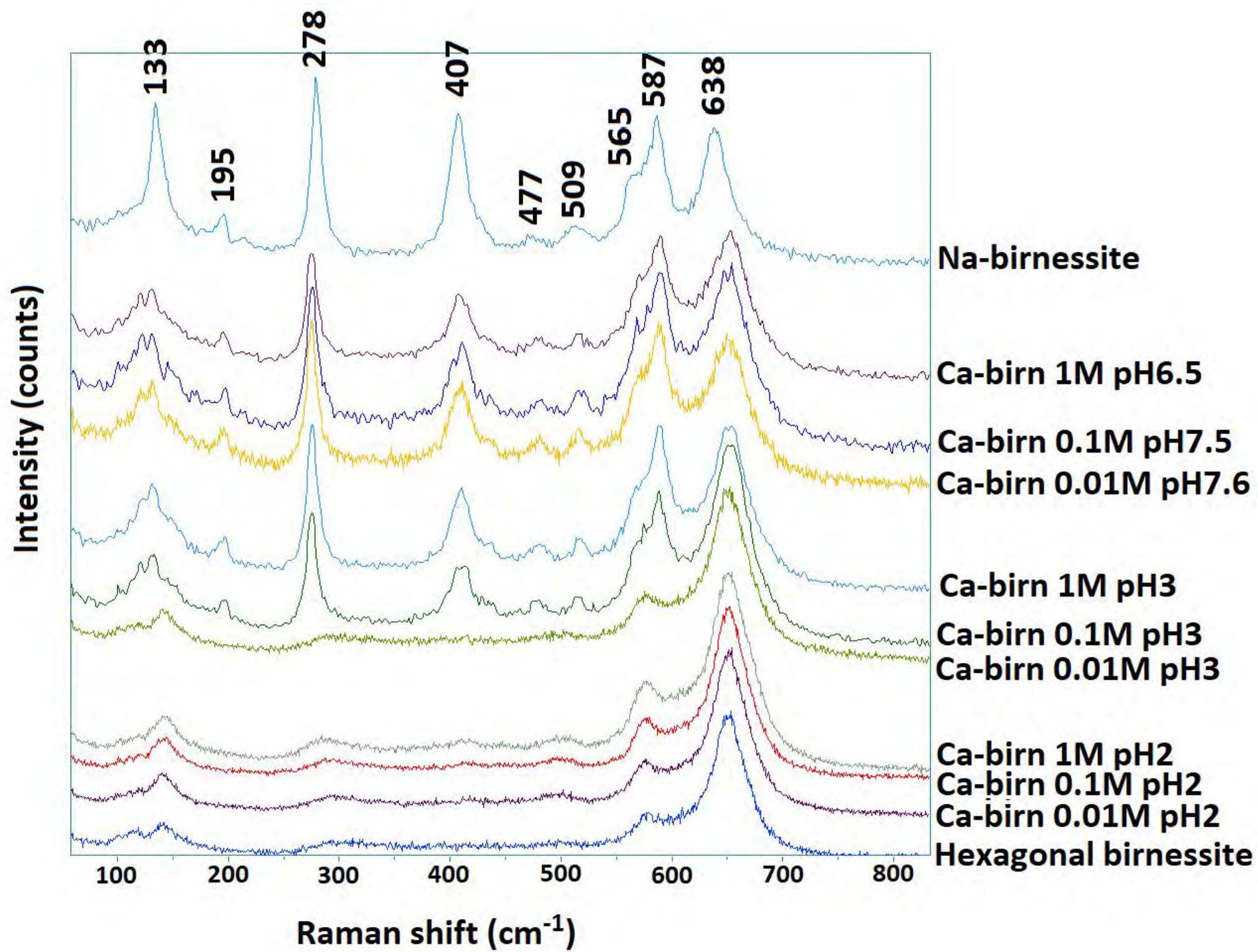


Figure 7

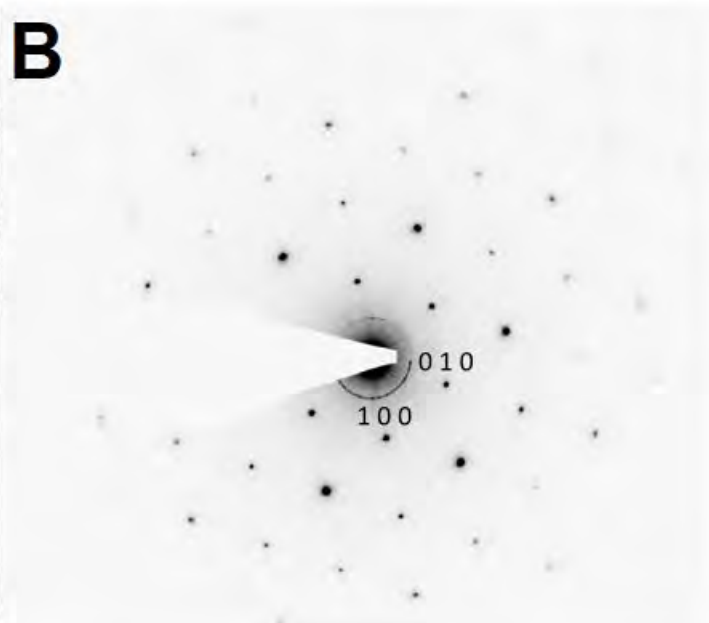
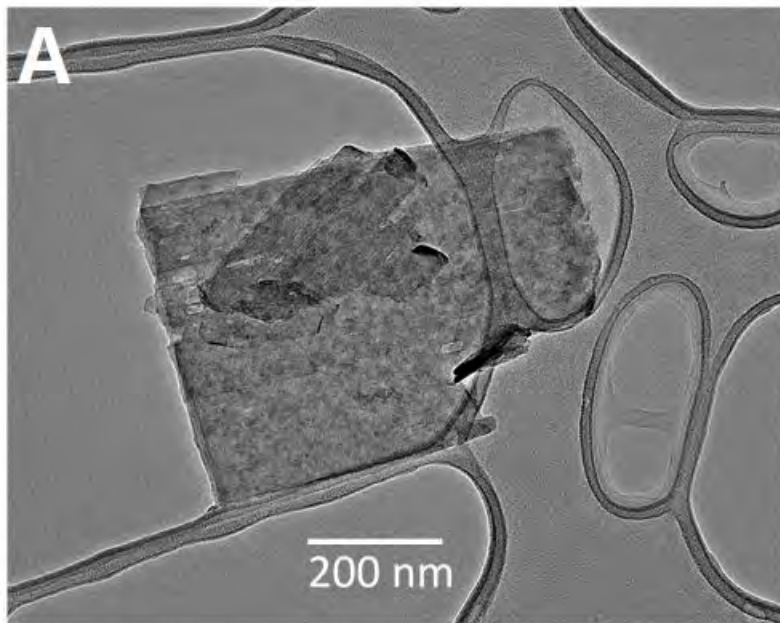


Figure 8a, b

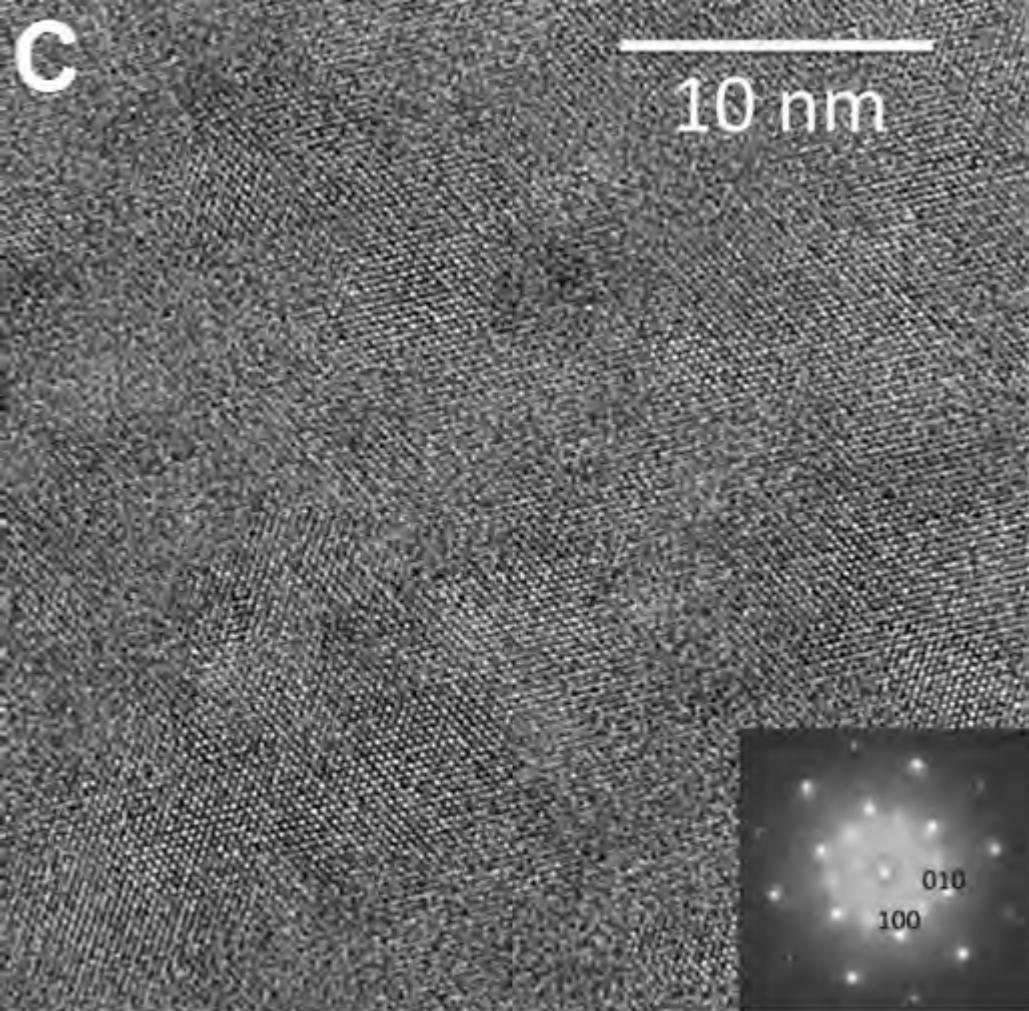


Figure 8c

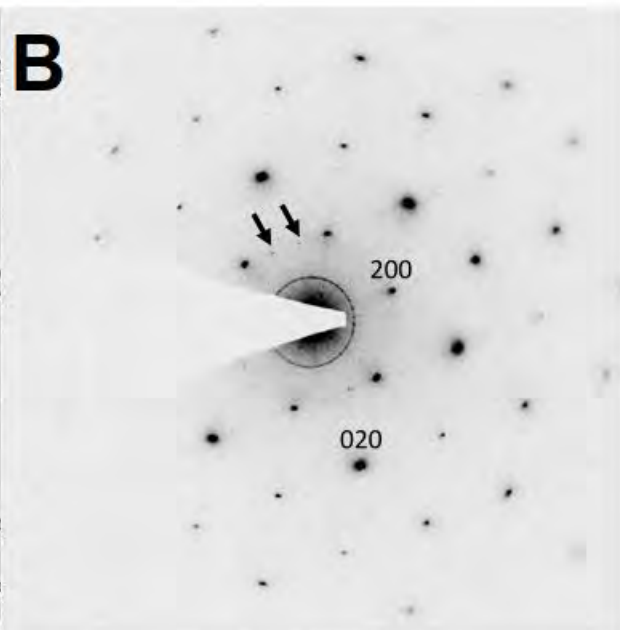
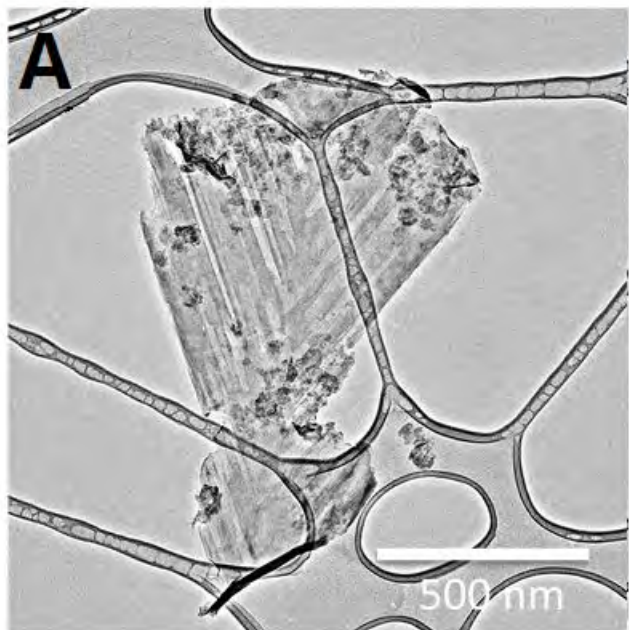


Figure 9a, b

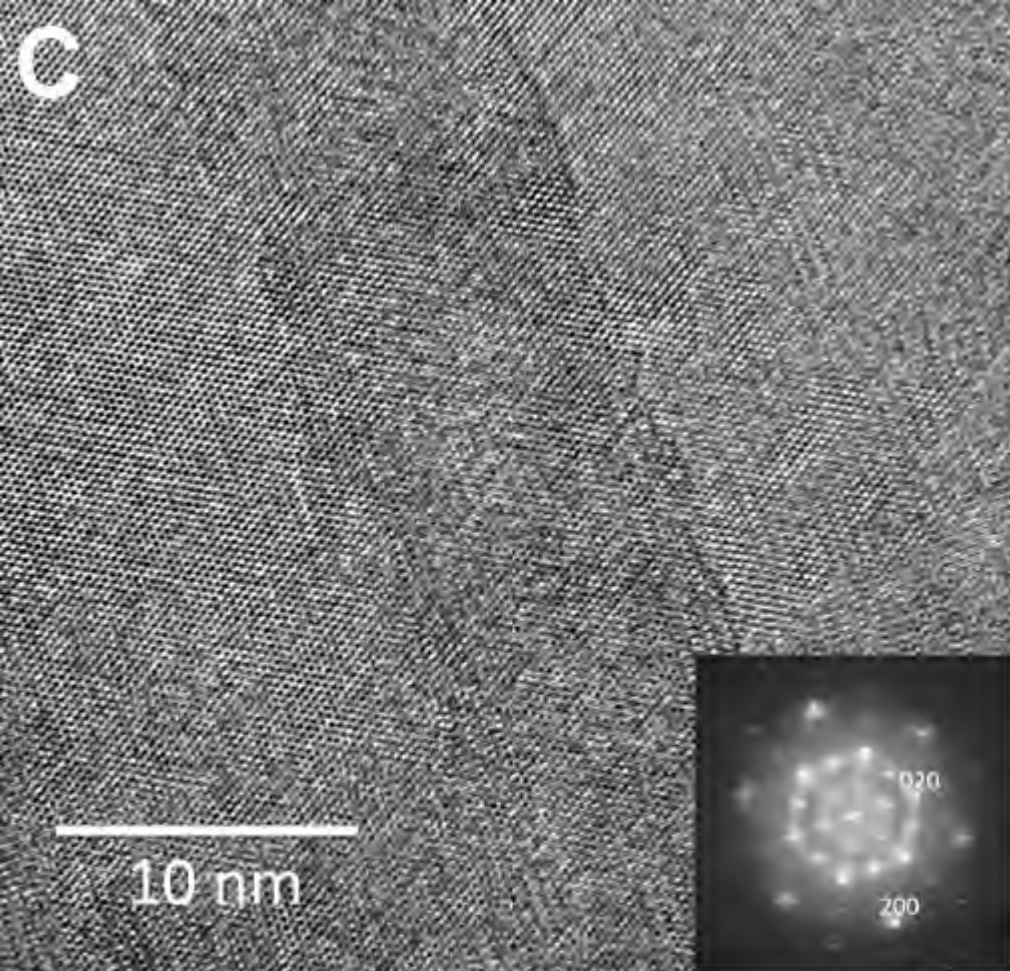


Figure 9c

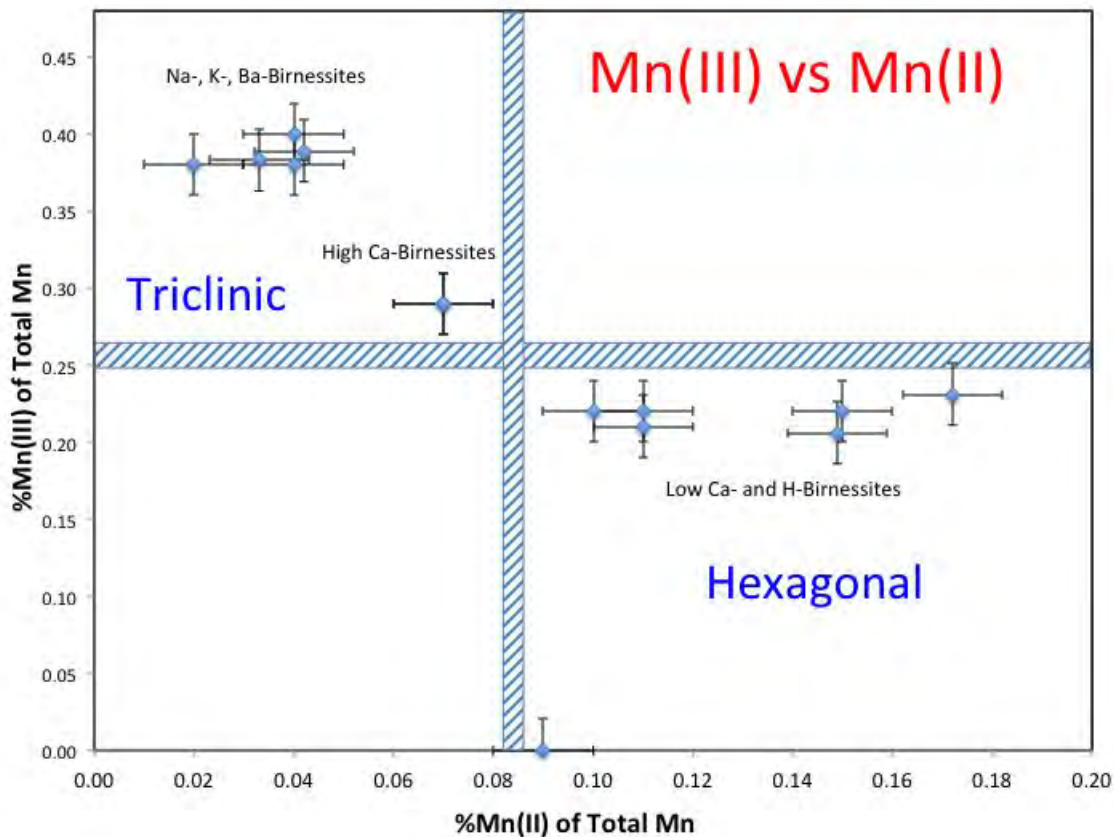


Figure 10